# Chem Soc Rev

## CRITICAL REVIEW

# Graphene-based composites

Xiao Huang,[a] Xiaoying Qi,[a] Freddy Boey[ab] and Hua Zhang*[ab]

Graphene has attracted tremendous research interest in recent years, owing to its exceptional properties. The scaled-up and reliable production of graphene derivatives, such as graphene oxide (GO) and reduced graphene oxide (rGO), offers a wide range of possibilities to synthesize graphene-based functional materials for various applications. This *critical review* presents and discusses the current development of graphene-based composites. After introduction of the synthesis methods for graphene and its derivatives as well as their properties, we focus on the description of various methods to synthesize graphene-based composites, especially those with functional polymers and inorganic nanostructures. Particular emphasis is placed on strategies for the optimization of composite properties. Lastly, the advantages of graphene-based composites in applications such as the Li-ion batteries, supercapacitors, fuel cells, photovoltaic devices, photocatalysis, as well as Raman enhancement are described (279 references).

[a] *School of Materials Science and Engineering, Nanyang Technological University, 50 Nanyang Avenue, Singapore 639798, Singapore. E-mail: hzhang@ntu.edu.sg, hzhang166@yahoo.com; Web: http://www.ntu.edu.sg/home/hzhang/*
[b] *Centre for Biomimetic Sensor Science, Nanyang Technological University, 50 Nanyang Drive, Singapore 637553*

*Hua Zhang studied at Nanjing University (BS, MS), and completed his PhD at Peking University (with Zhongfan Liu) in 1998. After postdoctoral work at Katholieke Universiteit Leuven (with Frans De Schryver) and Northwestern University (with Chad Mirkin), and working at NanoInk Inc. (US) and the Institute of Bio-engineering and Nanotechnology (Singapore), he joined Nanyang Technological University in July 2006. He was promoted to a tenured associate*

**Hua Zhang**

*professor in March 2011. He is an Associate Editor of the International Journal of Nanoscience, on the Editorial Board of NANO, and on the Advisory Committee of IOP Asia-Pacific. His research interests focus on carbon materials (graphene and CNTs) and their applications; controlled synthesis, characterization and application of novel nanomaterials; and surface fabrication from the micro- to nanometre scale, etc. He has published 25 patent applications, 3 book chapters, more than 130 papers with over 2400 citations and an H-index of 26. He has been invited to give more than 70 Keynote Lectures and Invited Talks in international conferences and universities, and serve as Session Chair. He has organized several international conferences and served as Symposium Chair.*

## 1. Introduction

The direct observation and characterization of a mechanically exfoliated graphene monolayer by Novoselov *et al.* in 2004[1] has sparked the exponential growth of graphene research in both the scientific and engineering communities. Graphene, a single-layer carbon sheet with a hexagonal packed lattice structure, has shown many unique properties, such as the quantum hall effect (QHE), high carrier mobility at room temperature ($\sim 10\,000$ cm$^2$ V$^{-1}$ s$^{-1}$),[1] large theoretical specific surface area (2630 m$^2$ g$^{-1}$),[2] good optical transparency ($\sim 97.7\%$),[3] high Young's modulus ($\sim 1$ TPa)[4] and excellent thermal conductivity (3000–5000 W m$^{-1}$ K$^{-1}$).[5] To further exploit these properties in various kinds of applications, versatile and reliable synthetic routes have been developed to prepare graphene and its derivatives, ranging from the bottom-up epitaxial growth[6–9] to the top-down exfoliation of graphite by means of oxidation, intercalation, and/or sonication.[10–13] In particular, the low-cost and mass production of chemically exfoliated graphene oxide (GO)[14–29] and reduced graphene oxide (rGO) sheets has been realized,[14–23,30–34] which possess many reactive oxygen-containing groups for further functionalization and tuning properties of GO or rGO sheets. With these added advantages, it is desirable to harness the useful properties of graphene and its derivatives in composites, through the incorporation with various kinds of functional materials. To date, graphene-based composites have been successfully made with inorganic nanostructures,[18–20,35–38] organic crystals,[39–40] polymers,[14,17,41,42] metal–organic frameworks (MOFs),[43–45] biomaterials,[46–48] and carbon nanotubes (CNTs),[49–53] and are intensively explored in applications such as batteries,[37,54–56] supercapacitors,[36,57–59] fuel cells,[60–63] photovoltaic devices,[19,33,64,65] photocatalysis,[66–69] sensing platforms,[46,47] Raman enhancement[70–72] and so on. In this

critical review, after introducing the properties and synthetic methods of graphene and its derivatives, graphene-based composites are discussed, with particular emphasis placed on their fabrication/synthesis methods, properties and applications.

## 2. Properties of graphene

### 2.1 Electronic properties

One of the most important properties of graphene is that its charge carriers behave as massless relativistic particles, or the Dirac fermions.[1] It has been demonstrated that graphene is a zero-gap 2D semimetal with a tiny overlap between valence and conductance bands, and charge carriers move with little scattering under ambient conditions.[1] It also exhibits a strong ambipolar electric field effect with the concentration of charge carriers up to $10^{13}$ cm$^{-2}$ and room-temperature mobilities of $\sim 10\,000$ cm$^2$ V$^{-1}$ s$^{-1}$, when the gate voltage is applied.[1] Besides, the suspended graphene shows low-temperature mobility approaching 200 000 cm$^2$ V$^{-1}$ s$^{-1}$ for carrier densities below $5 \times 10^9$ cm$^{-2}$, which is not observable in semiconductors or non-suspended graphene sheets.[73] Additionally, an unusual half-integer quantum Hall effect (QHE) for both electron and hole carriers in graphene has been observed by adjusting the chemical potential with the use of the electric field effect.[74,75] Such QHE can be observed at room temperature as well,[76] and the fractional QHE was obtained when suspended graphene devices were probed, which allows for the isolation of the sample from substrate-induced perturbations.[77]

### 2.2 Optical properties

The measured white light absorbance of suspended single-layer graphene is 2.3% with a negligible reflectance ($< 0.1\%$), and this absorbance increases linearly with the layer numbers from 1 to 5.[3] The measured values and the observed linearity are in consistence with the theoretical calculation results obtained with a model of non-interacting massless Dirac fermions. It shows that the dynamic conductivity of graphene in the visible range, $G$, only depends on the universal constants, i.e. $G \approx \pi e^2/2h$, where $c$ is the speed of light, $h$ is Planck's constant.[78] The transparency of graphene only depends on the fine-structure constant $\alpha = 2\pi e^2/hc$, which describes the coupling between the light and relativistic electrons. The absorbance of $n$-layer graphene can thus be simply expressed as $n\pi\alpha$. However, deviation from this behavior is found with the incident photons with energy less than 0.5 eV (or wavelength larger than $\sim 2480$ nm), which is attributed to the effects of finite-temperature, doping, and intra-band transitions.[79]

The ultrafast optical pump–probe spectroscopy has been applied to study the carrier dynamics and relative relaxation timescales of graphene layers grown on SiC.[80] An initial fast relaxation transient (70–120 fs) followed by a slower relaxation process (0.4–1.7 ps) has been identified, which is associated to the carrier–carrier intra-band and carrier–phonon inter-band scattering process, respectively. With the help of infrared spectroscopy, it is found that the inter-band transitions and optical transitions of monolayer and double layer graphene are layer-dependent and can be modulated through the electrical gating, which holds promise for the infrared optics and optoelectronics.[81]

### 2.3 Thermal properties

The thermal conductivity of single-layer suspended graphene at room temperature has been measured as 3000–5000 W m$^{-1}$ K$^{-1}$ depending on the size of the measured graphene sheet.[5] It is supported on amorphous silica, a case similar to the practical application, the measured thermal conductivity of graphene is $\sim 600$ W m$^{-1}$ K$^{-1}$, about one order lower than that of the suspended graphene sheet.[82] This reduction in thermal conductivity is attributed to the leaking of phonons across the graphene–silica interface and strong interface-scattering. Nevertheless, this value is still about 2 times and 50 times higher than copper and silicon, respectively, which are used in the electronics today.

### 2.4 Mechanical properties

The intrinsic mechanical properties of free-standing mono-layer graphene membranes were measured based on the nanoindentation using atomic force microscopy (AFM).[4] The breaking strength is 42 N m$^{-1}$ and the Young's modulus is 1.0 TPa, suggesting the strongest material ever measured. Theoretical work has been carried out to investigate the mechanical properties of zigzag graphene and armchair graphene nanoribbons, suggesting that the critical mechanical loads for failure and buckling of armchair ribbons are smaller than those for zigzag ribbons.[83] In addition, external mechanical loads can change the electronic properties of graphene, such as field emission performance.[83,84] By employing a cantilever beam, single-layered graphene can be subjected to various degrees of axial compression.[85] The uptake of stress and the compression buckling strains of different geometries have thus been measured. It is found that the mechanical response is related to the Raman shift of the G or 2D phonons of graphene.

The elastic deformation of functionalized graphene sheets (FGSs), or chemically reduced graphene oxide (rGO), has also been studied by AFM.[86] After repeatedly folding and unfolding of the FGSs multiple times, the folding lines were found to appear at the same locations, which can be attributed to the pre-existing kinks or defect lines in the FGSs.

## 3. Synthetic methods

Till now, tremendous efforts have been made to develop synthetic methods for graphene and its derivatives, not only to achieve high yield of production, but also to realize the solution or thin film based process. These methods can be generally classified as the bottom-up and top-down approaches. Table 1 summarizes and compares the typical synthetic methods for graphene and its derivatives. The bottom-up approach involves the direct synthesis of graphene materials from the carbon sources, such as the chemical vapor deposition (CVD), which is a typical method used to grow large-area, single and few-layer graphene sheets on metal substrates, e.g. Ni, Ru, and Cu.[6–9,49] Plasma enhanced CVD (PECVD) is able to grow single-layer graphene with high throughput at shorter reaction time and lower deposition temperature compared to the CVD process.[87] Besides, graphitization of carbon-containing

**Table 1** Comparison of various methods for preparation of graphene and its derivatives

| Methods | Conditions | Yield and properties | Ref. |
| --- | --- | --- | --- |
| *Bottom-up approaches* | | | |
| CVD | Carbon sources: $CH_4$, $H_2$<br>Substrate: Ni, Ru, Cu<br>Temperature: 1000 °C | Sheet size of up to a few tens of micrometres. | 6–8 |
| PECVD | Carbon source: $CH_4$, $H_2$<br>Substrate: Cu<br>Temperature: 650 °C | Large area of more than 1 cm of monolayer graphene | 87 |
| Graphitization | Substrate: 6H-SiC(0001)<br>Temperature: 1280 °C | Grain size: up to 50 μm long, 1 μm wide | 89 |
| Solvothermal | Reagents: Na and ethanol<br>Temperature: 220 °C | Folded graphene structures<br>Bulk conductivity: $\sim$0.05 S m$^{-1}$ | 90 |
| Organic synthesis | Thermal fusion of polycyclic aromatic hydrocarbons at 1100 °C | For a 30 nm thick film on quartz, conductivity: 20 600 S m$^{-1}$, sheet resistance: 1.6 kΩ m$^{-2}$ | 91 |
| *Top-down approaches* | | | |
| Liquid exfoliation of graphite | Intercalate: NMP | Single-layer yield: 7–12 wt% after purification<br>Film conductivity: $\sim$6500 S m$^{-1}$ | 11 |
| | Intercalate: SDBS | Film conductivity: $\sim$35 S m$^{-1}$<br>Single-layer yield: $\sim$3% with a size of $\sim$1 μm | 13 |
| | Intercalate: ternary potassium salt | Graphene ribbons with lengths of $\sim$40 μm. | 12 |
| Thermal exfoliation and liquid intercalation | Thermal exfoliation at 1000 °C<br>Intercalates: oleum and TBA | Single-layer yield: $\sim$90% after purification<br>Size: $\sim$250 nm<br>Resistance of single sheet with 100 nm in width: 10–20 kΩ | 98 |
| Electrochemical exfoliation | 1-Octyl-3-methyl-imidazolium hexafluoro-phosphate as electrolyte; graphite rods as electrodes | Sheet size: 500 × 700 nm | 99 |
| Chemical reduction of GO | Reduction agent: hydrazine | Sheet resistance of graphene paper: 7200 S m$^{-1}$ | 31 |
| | Deoxygenation agent: KOH or NaOH<br>Temperature: 50–90 °C | Incomplete removal of oxygen-containing groups | 109 |
| | Reduction agent: bovine serum albumin | To be used as template for nanoparticle synthesis | 111 |
| | Reduction agent: vitamin C<br>Temperature: 95 °C | Film conductivity: up to 7700 S m$^{-1}$ | 133 |
| | Reduction *via* bacteria respiration | Film resistance decreased up to $10^4$ after reduction | 134 |
| | Reduction agent: hydriodic acid and acetic acid | Sheet resistance: pellets dried after solution reduction: 30 400 S m$^{-1}$ | 32 |
| | In solution at room temperature or in vapor at 40 °C | Thin film after vapor reduction: 7850 S m$^{-1}$ | |
| | Sonolytic reduction: ultrasonication at 211 kHz for 30 min | Formation of 1–4 layers of rGO | 127 |
| | Microwave-assisted reduction in the presence of hydrazine | Formation of 1–8 layers of rGO with size up to a few micrometres | 128 |
| Thermal reduction of GO | 220 °C in air for 24 h | Film sheet resistance: 8 kΩ sq$^{-1}$ | 124 |
| | 150 °C in DMF for 1 h | Film resistance: 6 kΩ | 119 |
| Photothermal reduction of GO | High pressure Hg lamp with $H_2$ or $N_2$ flow | Sheet size: $\sim$1 um<br>Single-sheet conductivity: 2000–20000 S m$^{-1}$ | 115 |
| | Pulsed xenon flash | Able to prepare a GO/rGO patterned film with a photomask<br>Sheet resistance of rGO area: $\sim$9.5 kΩ sq$^{-1}$ | 126 |

substrates, such as SiC, can give rise to single-layer and few-layer graphene films as well through the high temperature annealing.[88,89] In addition to these methods based on the solid-phase deposition, graphene is also obtainable *via* the wet chemical reaction of ethanol and sodium followed by pyrolysis,[90] or through the organic synthesis to give graphene-like polyaromatic hydrocarbons.[91,92]

Different from the bottom-up approaches, the top-down approaches are advantageous in terms of high yield, solution-based processability, and ease of implementation, which have been demonstrated by means of intercalation, chemical func-tionalization, and/or sonication of bulk graphite. The first observation of exfoliated graphite dates back to 1840 by Schafhaeutl, when $H_2SO_4$ was used for the intercalation.[93] Since then, a number of chemical species have been found to form intercalated compounds with graphite.[94–97] Further attempts, combining the intercalation and sonication, have

realized isolation and dispersion of graphene sheets by using intercalates such as *N*-methyl-pyrrolidone (NMP)[11] and sodium dodecylbenzene sulfonate (SDBS)[13] in non-aqueous and aqueous solutions, respectively. Re-intercalation of thermally exfoliated expandable graphite (EG) with oleum (fuming sulfuric acid with 20% free $SO_3$) and tetrabutyl-ammonium hydroxide (TBA) has also produced single-layer graphene sheets with a yield of $\sim$90% after purification.[98] Even without sonication, ternary potassium salt-intercalated graphite readily gives isolated graphene sheets in NMP.[12] Additionally, electrochemical exfoliation of graphite has also achieved graphene nanosheets in ionic liquids.[99] Unfortu-nately, the aforementioned methods face drawbacks such as the low yield of single-layer production,[13] expensive intercalates,[11] and residual surfactant induced low conductivity. Therefore, an alternative approach, the reduction of highly oxidized graphene oxide (GO) sheets from the exfoliated

graphite oxide has been developed,[10] and mostly employed to prepare reduced GO (rGO), chemically converted graphene (CCG), or functionalized graphene sheets (FGS). The graphite oxide is obtained by the Hummers method *via* the reaction of graphite with a mixture of potassium permanganate ($KMnO_4$) and concentrated sulfuric acid ($H_2SO_4$).[14–23] The exfoliated GO sheets are thus highly oxidized and featured with the residual epoxides, hydroxides and carboxylic acid groups on their surfaces.[100,101] So far, various types of reduction methods have been reported to obtain rGO sheets, such as the chemical reagent reduction,[14–22,31,33,102–112] photochemical reduction,[113–116] thermal reduction,[117–124] photothermal reduction,[125,126] sonolysis,[127] microwave-assisted reduction[128] and electrochemical reduction.[129–132] Among these methods, the chemical reduction is the most versatile one with many reduction agents being used, such as hydrazine,[14–22,31,33,102–108] strong alkaline media,[109] vitamin C or ascorbic acid,[110,133] bovine serum albumin (BSA),[111] bacterial respiration,[134] and hydriodic acid.[32,135] To date, the rGO sheets reduced by hydriodic acid and acetic acid have shown the best electronic conductivity (up to $30\,000$ S m$^{-1}$).[32] Due to the less toxicity of hydriodic acid, this method is expected to replace the hydrazine reduction for the mass production of rGO dispersions and fabrication of rGO thin films. Despite the fact that the conductivity of rGO is orders lower compared to the pristine graphene due to the presence of residual oxygenated groups and defects, the reactive surfaces of GO and rGO provide the tunability in electronic and optoelectronic properties *via* chemical reactions,[118,136,137] and the feasibility for composite incorporation.[138]

## 4. Graphene–inorganic nanostructure composites

In the last few decades, huge efforts have been made to synthesize inorganic nanostructures with controlled shape, size, crystallinity and functionality. These materials are widely employed in applications like electronics, optics, electrochemical energy conversion and storage, solar energy harvesting, and so on. In order to further enhance their properties, a great number of inorganic nanostructures have been composited with graphene and its derivatives, which include metals like Au,[20,35,111,114,127,139–146] Ag,[20,146–150] Pd,[128,141,146,151,152] Pt,[111,141,146,153] Ni,[154] Cu,[128] Ru[155] and Rh;[155] oxides like $TiO_2$,[67,68,113,156–162] ZnO,[19,163–165] $SnO_2$,[166,167] $MnO_2$,[168,169] $Co_3O_4$,[54,55,170,171] $Fe_3O_4$,[172–175] NiO,[176] $Cu_2O$,[18,102,177] $RuO_2$,[59] and $SiO_2$;[178] chalcogenides like CdS[179–182] and CdSe.[183,184] The fabrication methods are generally classified as the *ex situ* hybridization, and *in situ* crystallization. Table 2 has summarized the typical synthetic methods for graphene–inorganic nanostructure composites and their related applications.

### 4.1 *Ex situ* hybridization

The *ex situ* hybridization involves the mixture of graphene-based nanosheets and pre-synthesized or commercially available nanocrystals in solutions. Before mixing, surface modification of the nanocrystals and/or graphene sheets is often carried out, so that they can bind through either the non-covalent interactions or the chemical bonding. For example, 2-mercaptopyridine modified Au nanoparticles (NPs)[145] or benzyl mercaptan-capped CdS NPs[179] have been successfully attached to GO or rGO surfaces *via* the π–π stacking. Alternatively, rGO sheets can be modified with adhesive polymers for anchoring the NPs, which has been demonstrated in the Nafion-coated rGO/$TiO_2$ composites.[161] Amphiphilic bio-polymers, such as bovine serum albumin (BSA) protein, have also been used to modify the rGO surface *via* the π–π interaction, which then serve as a "universal" adhesive layer to absorb Au, Ag, Pt and Pd NPs.[146]

Instead of decorating NPs on GO/rGO surfaces, GO/rGO sheets can wrap around the oxide NPs for specific applications such as the Li-ion battery.[55] As reported, after the positively charged $SiO_2$ or $Co_3O_4$ NPs (modified by aminopropyl-trimethoxysilane, APS) are encapsulated by negatively charged GO sheets through the electrostatic interaction, the GO can be *in situ* reduced to rGO subsequently without destroying the sheet-encapsulated-particle structures.

### 4.2 *In situ* crystallization

Although the *ex situ* hybridization is able to pre-select nano-structures with desired functionalities, it sometimes suffers from the low density and non-uniform coverage of the nano-structures on the GO/rGO surfaces.[145] In contrast, the *in situ* crystallization can give rise to uniform surface coverage of nanocrystals by controlling the nucleation sites on GO/rGO *via* surface functionalization. As a result, the continuous film of NPs on graphene surfaces can be realized.

**4.2.1 Chemical reduction method.** Chemical reduction is the most popular strategy for synthesis of metal nano-structures. Precursors of noble metals, such as $HAuCl_4$, $AgNO_3$, $K_2PtCl_4$ and $H_2PdCl_6$, can be simply *in situ* reduced by reduction agents like amines, $NaBH_4$, and ascorbic acid. For example, graphene–Au NP composites can be obtained by the reduction of $HAuCl_4$ with $NaBH_4$ in a rGO-octadecyl-amine (ODA) solution.[35] However, since rGO contains much less residual oxygen-containing functional groups than GO, it is restricted to aqueous solution based processes. To address this problem, 3,4,9,10-perylene tetracarboxylic acid (PTCA)-modified rGO sheets have been used as templates for the *in situ* reduction of $HAuCl_4$ with amino-terminated ionic liquid (IL-NH2). Because of the additional carboxylic groups from PTCA, the resulting rGO–Au NP composites are water soluble and give a dense coverage of NPs.[139]

Anisotropic metal nanostructures, such as nanorods[143,185] and snowflakes,[142] have also been synthesized on rGO or GO surfaces *via* chemical reduction. For example, Au nanorods can be prepared on rGO films or seed-modified rGO films, by using a shape-directing surfactant, cetyl trimethylammonium bromide (CTAB), to facilitate the one dimensional growth of the nanorods. Very recently, by using GO as a synthetic template, we have synthesized square-like Au nanosheets with an edge length of 200–500 nm and a thickness of ∼2.4 nm (Fig. 1A).[38] These Au nanosheets display the unique hexagonal close packed (hcp) structure. This is the first time to directly synthesize hcp Au nanostructures by the wet chemical method.

Besides the single-phased metal structures, Pt-on-Pd bimetallic nanodendrites on polyvinylpyrrolidone (PVP)-modified rGO

**Table 2** Comparison of typical synthetic methods for graphene–inorganic nanostructure composites and their related applications

| Materials | Synthetic routes | Applications | Ref. |
|---|---|---|---|
| Au/GO or rGO | *Ex situ*: π–π stacking *via* 2-mercaptopyridine | Catalysis, SERS | 145 |
| | *Ex situ*: π–π stacking *via* bovine serum albumin | | 146 |
| | *In situ*: photochemical reduction | | 114 |
| | *In situ*: reduction by hydroxyl-amine | Raman enhancement | 142 |
| | *In situ*: sonolytic reduction in poly(ethylene glycol) at 211 kHz | | 127 |
| Au/rGO | *In situ*: reduction by $NaBH_4$ | Plasmonics | 35 |
| | *In situ*: reduction by amino terminated ionic liquid; perylene-modified rGO | Electrocatalysis | 139 |
| | *In situ*: reduction by sodium citrate | SERS | 144 |
| | *In situ*: reduction by ascorbic acid in the presence of CTAB | Raman enhancement | 185 |
| | *In situ*: microwave assisted reduction | | 128,190 |
| Au/pristine graphene | *In situ*: thermal evaporation | Identification of layer number of pristine graphene | 189 |
| Ag/GO or rGO | *Ex situ*: π–π stacking *via* bovine serum albumin | | 146 |
| | *In situ*: reduction by $NaBH_4$ | | 150 |
| | *In situ*: electroless deposition | SERS | 20 |
| Ag/TiO$_2$/rGO | *In situ*: Ag is reduced by the photo-generated electrons from $TiO_2$/rGO | | 187 |
| Ag/rGO | *In situ*: microwave assisted reduction | | 128 |
| Pt or Pd/GO or rGO | *Ex situ*: π–π stacking *via* bovine serum albumin | | 146 |
| Pd/rGO | *In situ*: microwave assisted reduction | | 128 |
| Pt-on-Pd/rGO | *In situ*: sequential reduction of $H_2PdCl_4$ with HCOOH, and $K_2PtCl_4$ with ascorbic acid | Eletrocatalysis | 186 |
| Cu/rGO | *In situ*: microwave assisted reduction | | 128 |
| Ru/rGO | *In situ*: microwave assisted reduction | Catalysis | 155 |
| Rh/rGO | *In situ*: microwave assisted reduction | Catalysis | 155 |
| CdS/rGO | *Ex situ*: π–π stacking *via* benzyl mercaptan | Optoelectronics | 179 |
| TiO$_2$/GO | *Ex situ*: non-covalent adhesion *via* solution mixing of P-25 TiO$_2$ and GO | DSSC | 156 |
| | *Ex situ*: non-covalent adhesion *via* solution mixing with the GO film | Photocatalysis | 158 |
| TiO$_2$/rGO | *Ex situ*: noncovalent adhesion *via* Nafion | DSSC | 161 |
| | *Ex situ*: self-assembly of TiO$_2$ nanorods and rGO at two-phase interface | Photocatalysis | 67 |
| | *In situ*: templated hydrolysis starting with TiCl$_3$ and titanium isopropoxide | Photocatalysis | 68 |
| | *In situ*: hydrolysis starting with TiCl$_3$ | Li ion battery | 157 |
| | *In situ*: hydrolysis starting with titanium butoxide | DSSC | 160 |
| | *In situ*: hydrothermal starting with P25 and GO | Photocatalysis | 162 |
| ZnO/rGO | *In situ*: electrochemical deposition | Photovoltaics | 19 |
| Cu$_2$O/rGO | *In situ*: electrochemical deposition | Photovoltaics | 18 |
| Cl-doped Cu$_2$O/rGO | *In situ*: electrochemical deposition | Optoelectronics | 102 |
| Co$_3$O$_4$/GO or rGO | *Ex situ*: electrostatic *via* aminopropyltrimethoxysilane | Li ion battery | 55 |
| | *In situ*: reduction of Co(OH)$_2$/GO at 450 °C | Li ion battery | 54 |
| Co$_3$O$_4$/rGO | *In situ*: microwave assisted reaction between urea and Co(NO$_3$)$_2$ | Supercapacitor | 170 |
| MnO$_2$/GO | *In situ*: redox reaction between MnCl$_2$ and KMnO$_4$ | Supercapacitor | 168 |
| | *In situ*: microwave assisted reaction between C and KMnO$_4$ | Supercapacitor | 169 |
| MnO$_2$/FGS | *In situ*: redox reaction between Na$_2$SO$_4$ and KMnO$_4$ | Li ion battery | 166 |
| SiO$_2$/GO or rGO | *Ex situ*: electrostatic *via* aminopropyltrimethoxysilane | | 55 |
| SiO$_2$/FGS | *In situ*: hydrolysis starting with TEOS | | 166 |
| SnO$_2$/FGS | *In situ*: redox reaction starting with SnCl$_2$ and H$_2$O$_2$ | Li ion battery | 166 |
| Fe$_3$O$_4$/rGO | *In situ*: hydrolysis starting with FeCl$_3$ | Li ion battery | 173 |
| Fe$_3$O$_4$/GO | *In situ*: redox reaction starting with FeCl$_2$, FeCl$_3$ and NaOH | Magnetic drug carrier | 175 |
| | *In situ*: reaction of ferric triacetylacetonate with GO in 1-methyl-2-pyrrolidone | Magnetic composite | 172 |
| NiO/graphene | *In situ*: sputtering | Nanocapacitor | 176 |
| RuO$_2$/rGO | *In situ*: redox reaction starting with RuCl$_3$ and GO | Supercapacitor | 59 |
| CdS/rGO | *In situ*: chemical bath deposition | Solar cell | 180 |
| CdS/rGO | *In situ*: hydrothermal starting with dimethylsulfoxide, GO and Cd(CH$_3$COO)$_2$ | Optoelectronics | 181 |
| CdSe/CVD-graphene | *In situ*: electrochemical deposition templated by a porous silica film | Optoelectronics | 183 |

sheets have been synthesized in a seed-mediated sequential process, where the Pd seeds were synthesized on rGO by the reduction of $H_2PdCl_4$ with HCOOH, and then Pt nanodendrites on the Pd seeds were formed by reducing $K_2PtCl_4$ with ascorbic acid (Fig. 1B).[186] In this work, the pre-synthetic functionalization of rGO with PVP has provided good solubility of the rGO sheets in aqueous solution, and high nucleation density of the Pd seeds.

As an alternative, the photochemical reduction has also been applied for synthesis of graphene–metal nanostructure composites.[114,187] For example, our group has synthesized the fluorescent Au nanodots (NDs, with size <2 nm) on thiol-modified GO/rGO surfaces by simply *in situ* reducing $HAuCl_4$ under light irradiation.[114] Especially, if octadecylthiol (ODT) is used to modify the rGO surfaces, the *in situ* synthesized Au NDs self-assemble into short ND-chains on the ODT-rGO surfaces (Fig. 1C), along the ⟨100⟩ direction of the graphitic lattice. This is due to the specific pattern formation of the long chain thiol molecules on the rGO surface, which in turn serves as a secondary template for the synthesis and self-assembly of Au NDs. In another approach, semiconductor nanoparticles loaded on GO/rGO sheets are employed to catalyze the reduction of metal ions. The excited state interaction between semiconductor and GO/rGO has been studied in
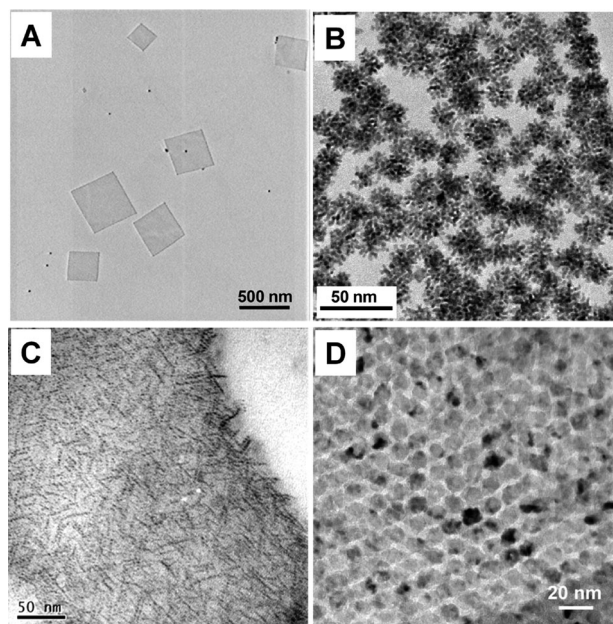
**Fig. 1** (A) TEM image of Au square sheets synthesized on GO. Reproduced from ref. 38. (B) TEM image of solution-synthesized Pt-on-Pd nanodendrites on rGO. Reproduced with permission from ref. 186. Copyright 2009, American Chemical Society. (C) TEM image of ordered Au NDs photochemically synthesized on rGO. Reproduced with permission from ref. 114. Copyright 2010, John Wiley & Sons, Inc. (D) TEM image of ordered CdSe NPs electrochemically deposited on a graphene sheet. Reproduced with permission from ref. 183. Copyright 2010, John Wiley & Sons, Inc.

the GO/ZnO system, based on the photoluminescence decay measurements.[165] It is shown that the lifetime of ZnO emission is decreased in the presence of GO sheets, indicating the fast electron transfer from ZnO to GO with a transfer-rate constant of $1.2 \times 10^9 \text{ s}^{-1}$. Such rapid electron transfer between semiconductor nanoparticles and GO/rGO makes their composites attractive photocatalysts. As an example, after GO sheets are photocatalytically reduced in the presence of light-excited $TiO_2$ nanoparticles, the resulting rGO/$TiO_2$ hybrid catalyst is subsequently used for photo-reduction of $Ag^+$. During this process, the photo-generated electrons from $TiO_2$ are rapidly captured by rGO and then transferred to reduce the absorbed $Ag^+$ ions on the rGO surface.[187]

In addition to metals, metal oxides, such as $RuO_2$,[54] $SnO_2$[166] and $MnO_2$,[168] can also form on GO/rGO surfaces *via in situ* reduction/oxidation. For example, GO/$RuCl_3$ was heated with a hot soldering iron in a $N_2$ atmosphere and *in situ* reduced to rGO/$RuO_2$ nanocomposites,[54] and $KMnO_4$ reacting with $MnCl_2 \cdot 4H_2O$ in the presence of GO sheets has led to $MnO_2$–GO composites.[168]

Microwave irradiation is a rapid and facile method to provide energy for chemical reactions. It can be used for the simultaneous formation of metal NPs (*e.g.* Cu, Pd, Au and Ag)[128] and reduction of GO. Additionally, the *in situ* microwave irradiation has been used to prepare metal oxide–rGO hybrids, such as rGO–$MnO_2$ NPs[169] and rGO–$Co_3O_4$ NPs.[170] In the former work, rGO serves as the carbon source to react with $KMnO_4$ under microwave irradiation to form

$CO_3^{2-}$, $HCO_3^-$, and $MnO_2$.[169] In spite of the ease of process and scalable production, the aforementioned microwave-assisted syntheses did not show the fine control over the size uniformity and surface distribution of NPs on rGO surfaces. More recently, the microwave irradiation was combined with ironic liquid (IL)-assisted dispersion of rGO to make Ru/rGO and Rh/rGO composites, which exhibit densely loaded Ru or Rh NPs with narrow size distributions of $2.2\pm0.4$ nm and $2.8\pm0.5$ nm, respectively.[155]

**4.2.2 Electroless deposition.** The electroless deposition of metals has been previously observed on single-walled carbon nanotubes (SWCNTs), where Au and Pt NPs formed on the side-walls of SWCNTs immediately after immersing the SWCNTs in solution of $HAuCl_4$ or $Na_2PtCl_2$.[188] Because the Femi level of SWCNT is higher (less negative) than the redox potential of Au or Pt, the SWCNT serves as the "cathode" to donate electrons for the nucleation of metal NPs. Based on the similar mechanism, we have shown that GO can be used to template the growth of Ag nanostructures *via* the electroless deposition, by simply heating GO films deposited on APTES-modified Si/$SiO_x$ substrates in $AgNO_3$ solutions.[20] In addition to GO, rGO sheets can also lead to the formation of Ag NPs due to the presence of many aromatic conjugated domains for electron donation. Importantly, the abundant residual oxygen-containing groups on GO provide more nucleation sites for metal nucleation, thus resulting in formation of smaller Ag NPs with higher density compared to using rGO as the template in the electroless deposition.

**4.2.3 Sol–gel methods.** The sol–gel process is a popular approach for preparation of metal oxide structures and film coatings, with the metal alkoxides or chlorides as precursors that undergo a series of hydrolysis and polycondensation reactions. It has been used to *in situ* prepare $TiO_2$,[68,157,160] $Fe_3O_4$[173] and $SiO_2$[166] nanostructures on FGS (or rGO) sheets. Taking $TiO_2$ as an example, the typical precursors used are $TiCl_3$,[157] titanium isopropoxide,[68] and titanium butoxide,[160] which have resulted in nanorods, NPs, or macro–mesoporous framework of $TiO_2$ depending on the different experimental conditions applied. The key advantage of the *in situ* sol–gel process lies in the fact that the surface $OH^-$ groups of the GO/rGO sheets act as the nucleation sites for the hydrolysis, so that the resulting metal oxide nanostructures are chemically bonded to the GO/rGO surfaces.

**4.2.4 Hydrothermal methods.** Hydrothermal is a powerful tool for synthesis of inorganic nanocrystals, which operates at elevated temperatures in a confined volume to generate high pressure. The one-pot hydrothermal process can give rise to nanostructures with high crystallinity without post-synthetic annealing or calcination, and at the same time reduce GO to rGO. Typically, $TiO_2$–rGO composites[162] and CdS–rGO composites have been prepared by the hydrothermal process. For example, after the mixture of GO and $Cd(CH_3COO)_2$ in dimethylsulfoxide (DMSO) was heated in an autoclave at 180 °C for 12 hours,[181] the simultaneous reduction of GO to rGO and the formation of CdS NPs were realized, with the DMSO acting as both the solvent and the sulfur source.

**4.2.5 Electrochemical deposition.** Direct electrochemical deposition of inorganic crystals on graphene-based substrates, without the requirement for post-synthetic transfer of the composite materials, is an attractive approach for thin film-based applications. Nanostructures of ZnO, $Cu_2O$ and CdSe[18,19,183] have been successfully deposited on rGO or CVD-graphene films. As an example, ZnO nanorods have been deposited on spin-coated rGO thin films on quartz, by using oxygen saturated aqueous solution of $ZnCl_2$ and KCl as the electrolyte.[19] This method has also been extended to deposit $Cu_2O$ nanostructures[18] as well as Cl-doped n-type $Cu_2O$[102] on rGO films, spin-coated on flexible polyethylene terephthalate (PET) substrates. In addition to the random deposition of nanostructures on rGO films, ordered nano-structure patterns can also be prepared by electrochemical deposition using porous template.[183] As reported, a layer of mesoporous silica film was first formed on the CVD-grown graphene sheets via a sol–gel process, and then CdSe NPs were electrochemically deposited on the graphene surface through the pores of the pre-coated silica film. After removing the silica film by HF etching, ordered CdSe NPs on graphene are revealed (Fig. 1D).

**4.2.6 Thermal evaporation.** The thermal evaporation has been utilized to deposit Au NPs on the pristine graphene and how the layer number of graphene affects the particle size and density of deposited Au NPs has been studied.[189] It is found that the particle density increases and size decreases with increasing the layer number of graphene. This interesting phenomenon has been attributed to two factors. First, the diffusion coefficient of deposited Au atoms varies on different surfaces, which governs the nucleation and growth of the Au islands. Second, the surface free energy of graphene depends on the layer number, which controls the interaction between graphene and the evaporated Au atoms, and in turn affects the surface absorption, desorption and diffusion of the Au atoms on graphene surface.[189]

**4.2.7 Ordered metal oxide–graphene composites via in situ self-assembly.** In contrast to the random stacking of graphene-based hybrid nanosheets, a novel method has been developed to prepare the ordered metal oxide–graphene hybrids by the surfactant assisted self-assembly.[166] In this work, the anionic surfactants were first mixed with rGO sheets, which attached to the hydrophobic domains of the surfactant micelles (Fig. 2A). After that, metal cations were introduced and bonded to the surfactants assembled on rGO, to give an ordered overall structure (Fig. 2B). In situ crystallization then took place, via redox or hydrolysis reactions, to result in the alternating layers of rGO/metal oxides, e.g. NiO, $SnO_2$, and $MnO_2$ (Fig. 2C and D). This assembly process is important in constructing layered composite materials for lithium ion batteries, which will be discussed in section 7.1.

# 5. Graphene–polymer composites

The graphene–polymer composites, based on the 3D arrangement and the kind of interaction between graphene sheets and polymers, can be classified into three types, i.e. graphene-filled
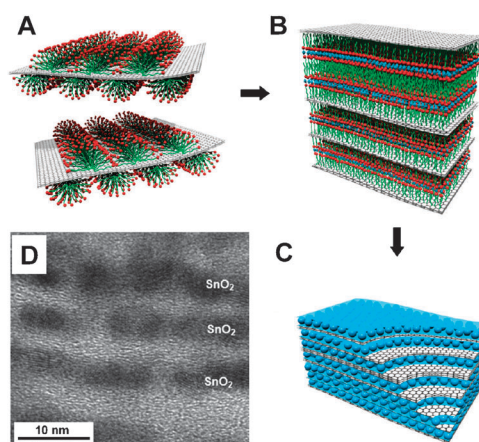


**Fig. 2** (A–C) Schematic illustrations of the self-assembly approach to prepare ordered metal oxide/rGO composites. (A) Adsorption of surfactant hemimicelles on the surfaces of the rGO or rGO stacks causes its dispersion in surfactant micelles in an aqueous solution. (B) The self-assembly of anionic sulfonate surfactant on the graphene surface with oppositely charged metal cation (e.g. $Sn^{2+}$) species and the transition into the lamella mesophase toward the formation of $SnO_2$ graphene nanocomposites, where hydrophobic rGO sheets are sandwiched in the hydrophobic domains of the anionic surfactant. (C) Layered metal oxide–rGO composites composed of alternating layers of metal oxide nanocrystals and rGO stacks after crystallization of metal oxide and removal of the surfactant. (D) High-magnification TEM of $SnO_2$/rGO composites. The layered structure of $SnO_2$ is composed of connected nanocrystalline $SnO_2$ with 4–5 nm diameter interspaced by rGO stacks. Reproduced with permission from ref. 166. Copyright 2010, American Chemical Society.

polymer composites, layered graphene–polymer films, and polymer-functionalized graphene nanosheets.

## 5.1 Graphene-filled polymer composites

Carbon-based materials, such as amorphous carbon and carbon nanotubes (CNTs), are conventional fillers for enhancing the electronic, mechanical and thermal properties of polymer matrices. CNT has been regarded as one of the most effective filler materials, but with relatively high cost. Graphene-based fillers are thus expected as a promising replacement or supplement to CNTs. In order to lower the content of the graphene filler, the dispersity and its bonding with the polymer matrix are important factors to achieve optimal properties of the composites. With this consideration in mind, graphene-filled polymer composites are commonly prepared by solution mixing,[42,191–195] melt blending,[196–198] and in situ polymerization.[199–210]

**5.1.1 Fabrication methods.** Solution mixing is the most straightforward method for preparation of polymer composites. The solvent compatibility of the polymer and the filler is critical in achieving good dispersity. Due to the residual oxygen-containing functional groups, GO can be directly mixed with water soluble polymers, such as poly(vinyl alcohol) (PVA), at various concentrations.[191,211] However, GO does not dissolve in non-polar solvents, and other forms of graphene such as expanded graphite (EG) and rGO show limited solubility in both organic and inorganic solvents. In order to overcome this problem, sonication has been used to

produce metastable dispersions of graphene derivatives, which are then mixed with polymer solutions, such as those of poly(methyl methacrylate) (PMMA),[192] polyaniline (PANi),[195] polycaprolactone (PCL),[193] and polyurethane (PU).[194,212] High-speed shearing combined with ice-cooling has also been applied to mix graphene-based fillers and the polymer matrices.[42] However, in the two approaches mentioned above, re-stacking, aggregation and folding of the graphene based nanosheets are unavoidable during the process, which significantly reduce the specific surface area of the 2D fillers. Thus, surface functionalization of graphene-based fillers before solution mixing must be carried out to provide them with good solubility in various kinds of solvents. As an example, phenyl isocyanate-modified GO sheets have shown improved dispersity in polystyrene (PS) solution in DMF. During the subsequent *in situ* reduction of GO, the polymer matrix prevents the re-aggregation of rGO sheets to retain a homogeneous suspension.[138]

Melt compounding utilizes both high-shear forces and high-temperature melting to blend the filler and matrix materials. Hence, it does not require a common solvent for the graphene filler and the polymer matrix. Polylactide (PLA)-exfoliated graphite (EG) composite[196] and PET–rGO graphene composite[197] were successfully prepared by using melt compounding. However, the high shear forces employed in melt compounding can sometimes result in the breakage of the filler materials, such as CNTs and graphene nanosheets.[198]

*In situ* polymerization is another often used method to prepare graphene-filled polymer composites, such as those with epoxy[199–201,213] and polyaniline (PANi).[202–206] In a typical process for preparation of graphene–epoxy composite, after the graphene based filler is mixed with epoxy resins under high-shear forces, a curing agent is added to initiate the polymerization.[199] The polymerization for PANi, on the other hand, is an oxidative process, thus an oxidative agent, such as ammonium persulfate, is used to facilitate the polymerization.[204] Alternatively, graphene–PNAi composite can be prepared by the *in situ* anodic electropolymerization.[207] For example, PANi has been directly deposited on the working electrode made from graphene paper in a three-electrode cell, with a solution containing aniline monomers as the electrolyte. In addition to the epoxy and PANi, graphene has been successfully incorporated in other polymer matrices, such as silicone,[208] PS[209] and poly(vinyl chloride/vinyl acetate) copolymer,[210] *via* the *in situ* polymerization.

**5.1.2 Property enhancement.** Electrical conductivity has shown significant improvement in graphene-filled polymers. Very low percolation thresholds have been achieved in various types of insulating matrices, for example, 0.15 vol% loading of rGO in poly(vinyl chloride/vinyl acetate) copolymer–graphene composites,[210] 0.47 vol% filler loading in PET–graphene composites (with a conductivity of 2.11 S m$^{-1}$ obtained at a loading of 3.0 vol%),[197] and 0.1 vol% filler loading in PS-functionalized graphene sheets (FGS) composites.[138] The effective property enhancement in these reports has been attributed to the large specific surface area and the $\pi$-conjugated 2D conducting surface of graphene-based sheets, their homogeneous dispersion in the polymer matrix,

and the filler–matrix interaction induced by the surface functional groups.

Besides the electrical conductivity, graphene-based fillers can improve the mechanical strength of the polymer as well, since the monolayer graphene is one of the strongest materials with a Young's modulus of 1.0 TPa and a breaking strength of 42 N m$^{-1}$.[4] By using solution mixing and vacuum filtration, the strong and ductile poly(vinyl alcohol)(PVA)–GO composite paper has been prepared, which shows a Young's modulus of 4.8 GPa and a tensile yield strength of $\sim$110 MPa with 3 wt% of the GO loading. Unfortunately, in the physically mixed composite, the relative movement between the filler and matrix cannot be avoided under external stresses, which limits the achievable maximum strength. To alleviate or solve this problem, it is necessary to chemically tailor the structure at the filler/matrix interface to facilitate the efficient load transfer. For example, GO filler was covalently bonded to isocyanated-PU matrix *via* the reaction between the oxygenated groups of GO and the isocyanate groups at the end of PU chains. This chemical bonding has led to the increase in the Young's modulus and hardness by $\sim$900% and $\sim$327%, respectively.[194]

The thermal stability is another important property for functional polymers, which can be improved by embedding materials with superior thermal properties like the graphene-based fillers. For example, FGS–PMMA composite gives an increase of 30 $°C$ in $T_g$ (glass transition temperature, above which chains of thermoplastic polymer begin to flow) with a loading of 0.05 wt% FGS, whereas the $T_g$ of poly(acrylonitrile)(PAN)–FGS composite increases more than 40 $°C$ with a loading of 1 wt% FGS,[42] which surpasses all other carbon-based nanofillers, such as the expanded graphite (EG) and the graphitic nanoplatelets (GNPs).[192] The superior performance of FGSs fillers, arises from the presence of larger amount of monolayer graphene sheets with wrinkled morphology and functionalized surfaces, which benefits the strong filler–matrix interaction (Fig. 3A and B).[42] Besides the thermoplastics, graphene-filled elastomers also exhibit enhanced thermal stability in terms of increased degradation temperature. Examples include the silicone–FGS composites with a 55 $°C$ increase in the degradation temperature with 0.25 wt% loading of the filler,[208] and the PLA–EG composite with the degradation temperature improved by 10 $°C$ with a loading of only 0.5 wt% of EG.[196]

Furthermore, the graphene-based filler materials have also enhanced the thermal conductivity of polymer matrices, provided that the single layer graphene has a thermal conductivity of up to $\sim$5000 W mK$^{-1}$ at room temperature.[214] When only
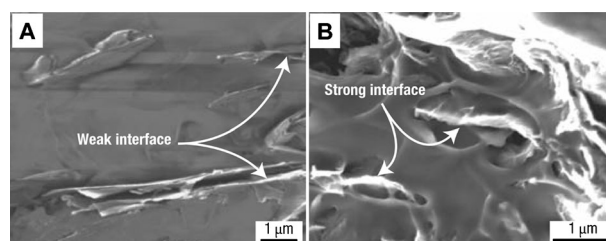


**Fig. 3** SEM images of (A) EG–PMMA and (B) FGS–PMMA showing fracture surface topography. Reproduced with permission from ref. 42. Copyright 2008, Nature Publishing Group.

0.25 wt% of FGSs were incorporated in the silicon foam matrix, the increase of 6% in the thermal conductivity was obtained.[208] In addition, epoxy with embedded few-layer graphene sheets ($\sim$25 vol%, layer number of $\sim$4) has displayed an increase in the thermal conductivity of more than 30 times at $k = 6.44$ W mK$^{-1}$.[199] This result outperforms many conventional fillers, such as Al, Ag and SiO$_2$, which require more than 50% loading to achieve the similar result.

## 5.2 Layered graphene–polymer films

In contrast to the graphene-filled polymer composites, where the graphene fillers are randomly distributed in the polymer matrices, graphene derivatives have also been composited with polymers in layered structures, which are fabricated for specific applications, such as the directional load-bearing membranes, and thin films for photovoltaic applications. For example, layer-by-layer (LbL) assembling *via* the Langmuir–Blodgett (LB) technique has been used to deposit GO sheets onto films of polyelectrolyte poly(allylamine hydrochloride) (PAH) and poly(sodium 4-styrene sulfonate) (PSS) multi-layers (Fig. 4A).[215] The resulting composited membrane shows enhanced directional elastic modulus by an order of magnitude, *i.e.* from 1.5 to 20 GPa with 8 vol% loading of the graphene (Fig. 4B). The similar strategy has been used to prepare multi-layer PVA–GO films, which also display improved elastic modulus and hardness.[216] Another application that requires layered graphene–polymer composites is in polymer-based photovoltaic devices.[217–219] These composite films are fabricated by the sequential spin-coating of functional components in the device configurations. For example, GO film and poly(3-hexylthiophene) (P3HT)/phenyl-C61-butyric acid (PCBM) blends are deposited layer after layer on ITO substrate, where the GO layer acts as the hole transport segment in the photovoltaic device.[218]

## 5.3 Polymer functionalized graphene nanosheets

Instead of being used as fillers to enhance the properties of polymers, graphene derivatives can be applied as 2D templates for polymer decoration *via* covalent and non-covalent functionalizations. The polymer coating, on the other hand, assists to improve the solubility of the graphene derivatives, and offers additional functionality to the resulting hybrid nanosheets.

The covalent functionalization of graphene derivatives is mainly based on the reaction between the functional groups of the polymers and the oxygenated groups on the GO or rGO surfaces. Esterification of the carboxylic groups in GO with the hydroxyl groups in PVA has been demonstrated in the synthesis of GO–PVA composite sheets.[220] The carboxylic groups on GO were also involved in the carbodiimide-catalyzed amide formation process to bind with the six-armed polyethylene glycol (PEG)-amine stars.[221] However, the carboxylic groups are mainly confined at the periphery of the GO sheets. In addition, the grafting of certain polymers requires the presence of non-oxygenated functional groups on GO, such as amine and chloride groups. Therefore, alternative strategies with additional chemical reactions have to be developed to modify GO/rGO surfaces with desired functional groups before the grafting of polymers. For example, after 4-bromophenyl groups were coupled on the rGO surface through the diazonium reaction, a fluorene–thiophene–benzothiadazole polymer was covalently grafted to the rGO surface through the Suzuki reaction *via* the 4-bromophenyl groups.[222] The pre-bonded diazonium group on rGO can also act as the initiator for atomic transfer radical polymerization (ATRP), based on which, PS has been successfully grafted onto the rGO sheet with controlled density.[223] Additionally, acyl-chlorinated GO sheets can further react and connect to triphenylamine-based polyazomethine (TPAPAM)[224] and MeOH-terminated P3HT,[225] and the APTES-modified GO surface can be further bonded with maleic anhydride-grafted polyethylene (MA-g-PE).[226]

As shown in the aforementioned examples, the covalent functionalization of polymers on graphene-based sheets holds versatile possibility due to the rich surface chemistry of GO/rGO. Nevertheless, the non-covalent functionalization, which relies on the van der Waals force, electrostatic interaction or π–π stacking,[227] is easier to carry out without altering the chemical structure of the capped rGO sheets, and provides effective means to tailor the electronic/optical property and solubility of the nanosheets. The first example of non-covalent functionalization of rGO sheets was demonstrated by the *in situ* reduction of GO with hydrazine in the presence
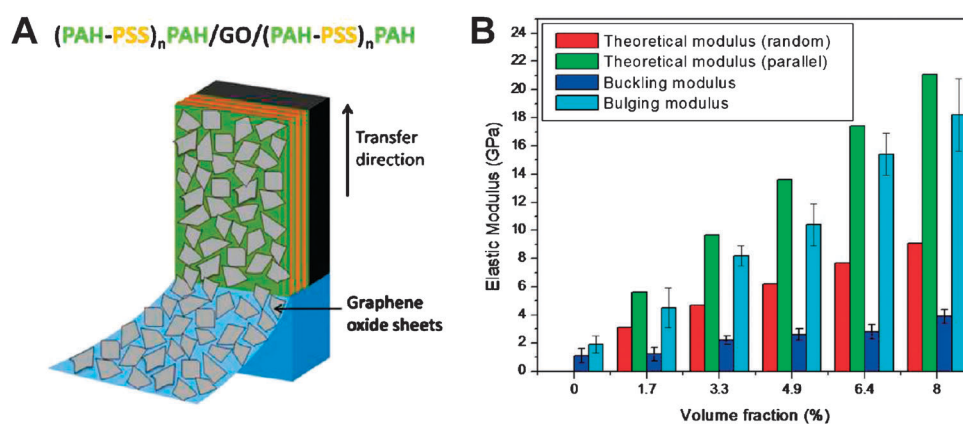


**Fig. 4** (A) Schematic illustration of fabrication and assembly of the free-standing GO-LbL film. (B) Plot showing the variation of elastic modulus calculated theoretically (under parallel and random orientation) and that obtained experimentally (using buckling and bulging measurements) with the volume fraction of GO. Reproduced with permission from ref. 215. Copyright 2010, American Chemical Society.
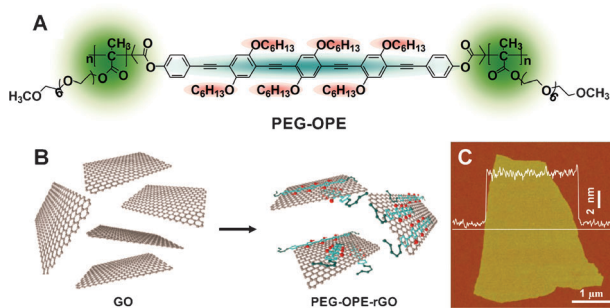
**Fig. 5** (A) Chemical structure of PEG–OPE. (B) Schematic illustration of fabrication of PEG–OPE stabilized rGO sheets. (C) Tapping-mode AFM image and cross-sectional analysis of PEG–OPE–rGO on mica. Reproduced with permission from ref. 14. Copyright 2010, John Wiley & Sons, Inc.

of poly(sodium 4-styrenesulfonate) (PSS),[228] in which the hydrophobic backbone of PSS stabilizes the rGO, and the hydrophilic sulfonate side groups maintains a good dispersion of the hybrid nanosheets in water. Later on, conjugated polyelectrolytes with various functionalities have been used to modify rGO nanosheets,[14,17,41] in the hope to achieve good solubility in different kinds of solvents, and at the same time acquire added optoelectronic properties. Our group has specially designed an amphiphilic coil–rod–coil conjugated triblock copolymer (PEG–OPE, chemical structure shown in Fig. 5A) to improve the solubility of graphene–polymer nanocomposites in both high and low polar solvents.[14] In the proposed configuration, the conjugated rigid-rod backbone of PEG–OPE can bind to the basal plane of the *in situ* reduced GO *via* the π–π interaction (Fig. 5B), whereas the lipophilic side chains and two hydrophilic coils of the backbone form an amphiphilic outer-layer surrounding the rGO sheet. As a result, the obtained rGO sheets with a uniformly coated polymer layer (Fig. 5C) are soluble in both organic low polar (such as toluene and chloroform) and water-miscible high polar solvents (such as water and ethanol).

## 6. Other graphene-based composites

Other than inorganic nanostructures and polymers, materials such as organic crystals,[39,40] metal–organic frameworks (MOF),[43–45] biomaterials,[46–48] and carbon nanotubes (CNTs)[50–53] have also been composited with graphene derivatives for various applications.

For example, $N,N'$-dioctyl-3,4,9,10-perylenedicarboximide (PDI)–graphene core/shell nanowires have been prepared through the π–π interaction, and used in organic solar cells.[39] Besides, peptide–graphene core/shell nanowires were prepared by mixing graphene aqueous solution and the organic peptide solution (diphenylalanine in 1,1,1,3,3,3-hexafluoro-2-propanol). After removal of peptide cores by calcination, the hollow graphene tubes were applied as supercapacitor electrodes.[40]

MOF, a recently emerging material, is promising in a number of gas purification and storage based applications, and has also been composited with GO/rGO sheets.[43–45] As an interesting example, benzoic acid-functionalized graphene has been found to act as a structure-directing template for the growth of MOF-5, which exhibits the wire-like structure along

its [220] direction. Along the long axis of the wire, the functionalized graphene sheets are periodically distributed, which are expected to impart photoelectric transport property to the insulating structure of MOF-5.[43]

Moreover, biomaterials like DNA hybridized with GO or rGO are used in fluorescent sensing platforms based on the fluorescence resonance energy transfer (FRET),[46,47] and biocompatible aptamer–GO composites can be applied in probing living cells.[48] Graphene–CNT composites have also been prepared *via* solution blending[50,51] or *in situ* CVD growth[53] to be applied in Li ion batteries,[51] transparent conductors,[50] and supercapacitors.[52,53]

## 7. Applications of graphene-based composites

### 7.1 Lithium ion batteries

The increasing demand from the current information-rich society to provide high efficient, low cost and green solutions for energy conversion and storage devices, has been constantly driving the development of battery systems, in particular, the rechargeable batteries. Li ion battery (LIB) is considered as one of the most promising storage systems, because of its high absolute potential against the standard hydrogen cell ($-3.04$ V) and its low atomic weight ($M = 6.94$ g mol$^{-1}$), which leads to the large energy density with a theoretical value of up to ~400 Wh kg$^{-1}$.[229,230] In addition to the traditional insertion-type (*e.g.* TiS$_2$ and LiCoO$_2$)[231,232] and alloying-type (*e.g.* Sn)[233] of electrode systems for insertion/extraction of Li, the conversion-type LIB has been intensively studied recently, which employs transition metal compounds (M$_a$X$_b$, M = Co, Ni, Fe, Cu *etc.*; X = O, S, P, N *etc.*) to facilitate the Li insertion/extraction through redox reactions (reaction (1)) between the ionic and metallic states of the metal, thus providing high capacities.[234]

$$M_aX_b + cLi^+ + ce^- \leftrightarrow Li_cX_b + aM \qquad (1)$$
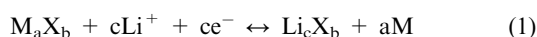
**7.1.1 Graphene–metal oxide nanostructures for LIBs.** The nanostructured M$_a$X$_b$ has been proven to be advantageous compared to micrometre-sized structures for LIBs, owing to the shortened diffusion length for both Li ions and electrons, and larger specific surface area for the electrode/electrolyte interaction.[235] However, drawbacks like poor conductivity, low packing density thus reduced volumetric energy density, as well as the expansion induced lose of contact points, remain problematic and require continuous development. Although graphene and its derivatives cannot effectively host Li *via* intercalation like in bulk graphite, they are able to store Li through the surface absorption and functional groups induced bonding,[236] and they possess high conductivity and large surface area. Therefore, many metal oxide nanostructures, like SnO$_2$,[166,167,237] Co$_3$O$_4$,[54,55] MnO$_2$,[56] TiO$_2$,[157,238] Fe$_3$O$_4$[173] and Cu$_2$O,[177] have been composited with graphene for LIBs.

Rapid capacity decay is usually observed in the pure metal oxide based anodes, due to problems like poor conductivity, structure degradation and expansion, and inter-particle agglomeration. Using graphene based materials as matrices for *in situ* synthesis and anchoring of the metal oxide nanostructures is anticipated to solve these problems. First of all, the incorporation of graphene maintains a good conducting network in the

hybrid electrode. This effect has been elucidated in a recent report on the $Mn_3O_4$/graphene based anode.[56] Although $Mn_3O_4$ is an attractive anode material for LIBs considering its low cost, abundance, and high theoretically value in capacity ($\sim$936 mAh g$^{-1}$), its low conductivity ($\sim 10^{-7}$–$10^{-8}$ S cm$^{-1}$) has limited its practical application with a measured capacity of 400 mAh g$^{-1}$.[56] Direct growth of $Mn_3O_4$ NPs on graphene sheets provides a good contact between the NPs and the 3D network of graphene, thus realizes efficient conduction of charge carriers. Consequently, the graphene/$Mn_3O_4$ hybrid anode affords a specific capacity of $\sim$900 mAh g$^{-1}$, about two times higher than that by using the pure $Mn_3O_4$. The same effect, arising from the conducting network of graphene sheets, has also been demonstrated in $SnO_2$/graphene,[237] $TiO_2$/graphene[157] and $Fe_3O_4$/graphene[173] electrodes.

By using graphene as templates, another attractive aspect is that the synthesized NPs can be evenly distributed on the graphene surfaces. In this way, the agglomeration of NPs can be considerably reduced and the large active surfaces of the NPs are able to participate in Li/electron diffusion more efficiently during the discharge/charge cycles. As a result, enhanced specific capacity and cycling performance have been achieved in systems like $Co_3O_4$/graphene[54] and $Cu_2O$/graphene[177] composites. In addition, the elastic and flexible graphene sheets can accommodate the volume expansion of the NPs upon Li insertion/extraction; whereas the NPs in turn prevent the re-stacking of the graphene layers.[173] More importantly, it has been shown that the structure integrity of the crystalline NPs on graphene can be maintained after many cycles of discharge/charge. As an example, the Li insertion/extraction in $SnO_2$ based anode usually involves a two phase process, i.e. in the first cycle, the $SnO_2$ reacts with Li$^+$ to give Sn and $Li_2O$; after that, Sn will not reverse back to $SnO_2$ but form SnLi$_x$ alloy for the rest cycles,[237,239] which leads to large volume change and rapid capacity decay. This problem can be overcome by using $SnO_2$/graphene hybrid anode, which shows a well maintained $SnO_2$ crystalline structure after 50 cycles.[167]

Although the graphene-based 2D templates have provided the good NP distribution on individual sheets, the graphene–NP hybrid sheets are randomly stacked to make electrodes, inevitably leading to the particle–particle aggregation. Thus, the ordered graphene–metal oxide composites[166] and graphene encapsulated metal oxide nanostructures[55] have been developed to further reduce the particle aggregation. In the former case, layers of graphene stacks and metal oxide NPs (e.g. $SnO_2$) are assembled alternatively through a surfactant assisted self-assembly process (Fig. 2 in section 4.2.7). Such highly ordered and stable structure of graphene/$SnO_2$ exhibits a specific energy density of $\sim$760 mAh g$^{-1}$, which is comparable to the theoretical value for $SnO_2$ without significant charge/discharge degradation.[166] However, most graphene stacks consist of multi-layer graphenes, which reduce the useful surface area of graphene and increase the carbon content in the composite. In an alternative approach, graphene sheets are made to wrap around NPs of $SiO_2$ or $Co_3O_4$ via the electrostatic interaction in the graphene encapsulated-metal oxide hybrids (Fig. 6A).[55] The graphene encapsulation is able to separate individual NPs from one another, which prevents the particle agglomeration, and maintains a conducting network to
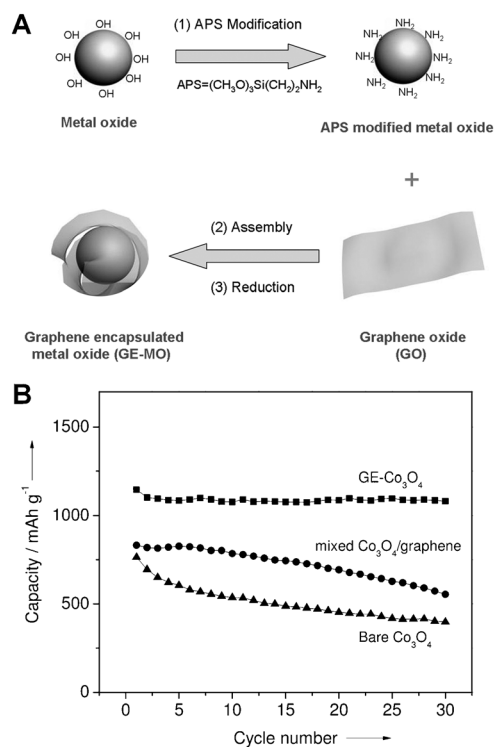


**Fig. 6** (A) Schematic illustration of fabrication of graphene-encapsulated metal oxide NPs. (B) Cycle performance of graphene-encapsulated $Co_3O_4$. Reproduced with permission from ref. 55. Copyright 2010, John Wiley & Sons, Inc.

effectively connect all NPs. The resulting graphene/$Co_3O_4$ based anode, with a low carbon content of <8.5 wt%, displays a very high capacity of 1100 mAh g$^{-1}$ in the first 10 cycles, and maintains at above 1000 mAh g$^{-1}$ even after 130 cycles (Fig. 6B).

### 7.1.2 Graphene–carbon nanotube or graphene–fullerene hybrid for LIB.

To date, besides the graphene–metal oxide based anode materials for LIBs, graphene–carbon nanotube (CNT) or graphene–fullerene ($C_{60}$) hybrid electrodes are also reported.[51] The graphene nanosheets (GNSs), prepared from reduction and re-assembly of oxidized GO sheets, consist of 6–15 re-stacked individual graphene monolayers. The GNSs show a specific capacity of $\sim$540 mAh g$^{-1}$, which is much larger than that of graphite due to the enlarged specific surface area after exfoliation. The energy storage property of this electrode can be further improved by mixing GNSs with nanocarbons, such as CNTs and $C_{60}$, to increase the spacings among the re-stacked GNSs. In this way, the additional voids for Li insertion/extraction are created in the mixtures, resulting in $\sim$40% increase in the specific capacity.
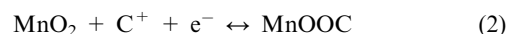
### 7.2 Supercapacitors

Supercapacitor, or ultracapacitor, is another type of electro-chemical energy storage device, which provides high power density (10 kW kg$^{-1}$), short charge/discharge time (in seconds), and long cycling life, as compared to the battery device.[240] Thus, supercapacitor is widely applied for powering the heavy vehicles, portable media players, personal computer (PC) cards, and so on. Generally, there are two types of

supercapacitors, in terms of their operation mechanisms.[241] One is the electrical double layer capacitor (EDLC), which stores energy *via* an electrostatic process, *i.e.* the charges are accumulated at the electrode/electrolyte interface through polarization. Hence, it is essentially important to use electrode materials with good conductivity and large specific surface areas in EDLCs, such as the activated carbon, CNTs, carbon nanofibers, and the emerging graphene-based 2D sheets. The graphene-based materials, in particular rGO, are advantageous in terms of the chemically active surface with large specific area, good conductivity, low cost, and mass production with solution-based processability as mentioned before. In addition, it is suggested that the aggregated graphene sheets exhibit an open-pore structure, which allows for the easy access of electrolyte ions to form electric double layers.[242] The first EDLC based on the chemically modified graphene, or rGO, was demonstrated by Ruoff and coworkers.[2] A specific capacitance of 135 F g$^{-1}$ in the aqueous electrolyte is obtained, which is comparable with the traditional carbon-based electrode materials.

The other type of supercapacitor is so called the *pseudo*-capacitor, which is based on the rapid redox reactions of the chemical species present in the electrode.[241] Commonly used electrode materials are metal oxides (*e.g.* RuO$_2$, NiO and MnO$_2$) and conducting polymers (*e.g.* Polyaniline, PANi and Polypryrrole, PPy). This type of electrode affords higher specific capacitance per unit surface area (1 to 5 F m$^{-2}$) compared to the porous carbon based EDL electrode (0.1 to 0.2 F m$^{-2}$).[242] However, the relatively high cost and low conductivity of metal oxides or conducting polymers have limited their applications. As a result, graphene derivatives and metal oxides or conducting polymers are combined and used as the hybrid type of supercapacitor (*i.e.* the combination of the EDLC and *pseudo*-capacitor).

**7.2.1 Graphene–metal oxide supercapacitors.** A number of metal oxides, such as ZnO,[57] SnO$_2$,[58] Co$_3$O$_4$,[170] MnO$_2$[168,169] and RuO$_2$,[59] have been composited with graphene derivatives to prepare electrodes for supercapacitors. Taking the graphene/MnO$_2$ hybrid electrode for example,[169] the MnO$_2$ NPs contribute to the energy storage *via* the redox reaction in between the III and IV oxidation states of Mn (reaction (2)), which involves the intercalation of alkali metal ions present in the electrolyte, *e.g.* Na$^+$. The rGO sheets, on the other hand, provide the capacitance through the electron double layer
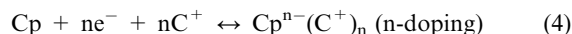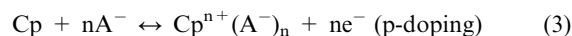
at the carbon surface, and meanwhile afford a conducting network for the anchored MnO$_2$ NPs and large surface area for the NP/electrolyte interaction, which leads to high *pseudo*-capacity with rapid charge–discharge rate. The resulting composite electrode shows a high specific capacitance of 310 F g$^{-1}$ at 2 mV s$^{-1}$ (228 F g$^{-1}$ at even 500 mV s$^{-1}$), about 3 times higher than that given by the pure rGO or MnO$_2$. Similarly, a graphene nanosheet (GNS)/Co$_3$O$_4$ supercapacitor displays a maximum specific capacity of 243.2 F g$^{-2}$ at a scan rate of 10 mV s$^{-1}$ in KOH aqueous solution, and ∼95.6% of the specific capacitance is retained after 2000 cycles.[170]

$$MnO_2 + C^+ + e^- \leftrightarrow MnOOC \quad (2)$$

where C$^+$ = Na$^+$, K$^+$ or Li$^+$

Compared to batteries, supercapacitors exhibit higher power density but lower energy density. In order to improve the energy density of a supercapacitor, while maintaining the high power density from the graphene/metal oxide hybrid electrode, an asymmetric capacitor system was employed by Cheng and coworkers.[243] In such a capacitor, graphene is incorporated as the negative electrode (a battery type) and MnO$_2$ nanowire/graphene composite (MGC) as the positive electrode (Fig. 7A). A high operating voltage (∼2.0 V) is thus made possible in this asymmetric set-up to give the high energy density (note that the energy is directly proportional to the square of the operating voltage across the cell). As a result, a maximum energy density of 30.4 Wh kg$^{-1}$ for this asymmetric capacitor is achieved, which is much higher than the results obtained from the symmetric one, *i.e.* with graphene (or graphene/MnO$_2$) as both the positive and negative electrodes (Fig. 7B).

**7.2.2 Graphene-conducting polymer supercapacitors.** Conducting polymers are attractive materials for supercapacitor electrodes, because they have moderate conductivity, *e.g.* 0.1–5 S cm$^{-1}$ for doped polyaniline (PANi),[244] fast charge–discharge kinetics and doping–undoping processes,[245] and flexibility for thin film based fabrications.[246] The power conversion and storage process in polymer-based capacitors involves the doping–undoping redox reactions, as shown in reactions (3) and (4):

$$Cp + nA^- \leftrightarrow Cp^{n+}(A^-)_n + ne^- \text{ (p-doping)} \quad (3)$$

$$Cp + ne^- + nC^+ \leftrightarrow Cp^{n-}(C^+)_n \text{ (n-doping)} \quad (4)$$

where Cp = conducting polymer; C$^+$ = cation; A$^-$ = anion.
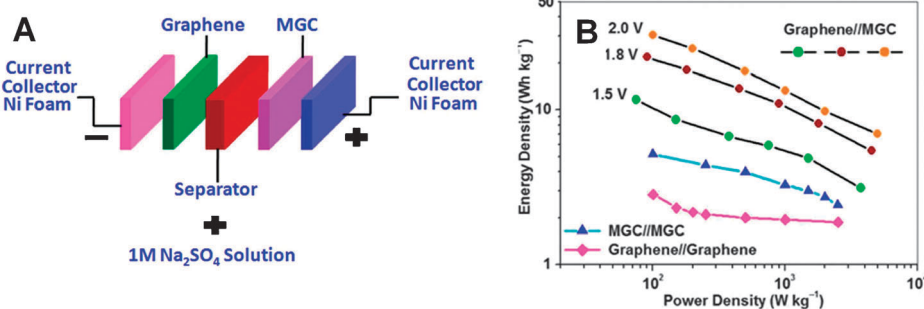


**Fig. 7** (A) Schematic of the assembled structure of asymmetric ECs based on MGC as the positive electrode and graphene as the negative electrode. (B) Ragone plot related to energy and power densities of graphene//MGC asymmetric ECs with various voltage windows, graphene//graphene and MGC//MGC symmetric ECs. Reproduced with permission from ref. 243. Copyright 2010, American Chemical Society.

Till now, PANi is one of the most employed polymers to be incorporated with GO or rGO sheets for super-capacitors.[195,202–207,247,248] In the GO–PANi composite, the doping process is realized by linking the carboxyl group of GO to the nitrogen of the PANi backbone.[205,206] Since PANi is synthesized on GO *via* the *in situ* polymerization, the oxygen-containing functional groups of GO can facilitate the nucleation of the polymer and give rise to good surface coverage of PANi and the strong $\pi$–$\pi$ interaction between the PANi backbone and the GO surface. As reported, with 1% mass loading of GO, the conductivity of the PANi based electrode is improved from 2 S cm$^{-1}$ (for pure PANi) to 10 S cm$^{-1}$, and a high specific capacitance of 531 F g$^{-1}$ (216 F g$^{-1}$ for the pure PANi) is obtained in the potential range of 0 to 0.45 V at a scan rate of 10 mV s$^{-1}$.[206] Besides the enhanced conductivity and capacitance, GO is also able to improve the cycling-stability of the composite electrode, because the flexible GO sheets can undertake mechanical deformation during the charge–discharge cycles to protect the PANi polymer from shrinkage and swelling.[205,248] For example, a hierarchical composite electrode of GO–PANi can retain 92% of the initial capacitance after 2000 cycles, whereas the initial capacitance of pure PANi electrode drops to 74%.[248]

Although the chemically modified graphene, or rGO, exhibits much better intrinsic conductivity as compared to GO, the rGO–PANi electrode has not shown any improved electrochemical performance compared to GO–PANi at a low GO/rGO content (< 20 wt%).[195,203] This is possibly because, the less amount of oxygenated functional groups on the surface of rGO compared to GO has caused the poor polymerization and distribution of PANi nanostructures, and less effective doping of PANi *via* the carboxyl groups.

### 7.2.3 Graphene–carbon nanotube (CNT) supercapacitors.

In graphene-based supercapacitors, re-stacking of graphene sheets can lead to the decrease of active surface area. To solve this problem, CNTs can be used as spacers to create nanopores among graphene layers, and at the same time provide good conductivity. For example, poly(ethyleneimine) (PEI)-modified rGO sheets mixed with acid-oxidized multi-walled CNTs to make hybrid carbon films gave an average specific capacitance of 120 F g$^{-1}$ at a high scan rate of 1 V s$^{-1}$.[52] The concept of using CNT spacers is further employed in a three dimensional (3D) CNT/graphene sandwich structure (CGS), in which CNTs are grown amongst the graphene layers *via* the CVD process (Fig. 8A and B).[53] The resulting Brunauer–Emmett–Teller (BET) surface area of the CGS is 612 m$^2$ g$^{-1}$, which is much higher than that of graphene (202 m$^2$ g$^{-1}$). A specific capacitance of 386 F g$^{-1}$ is thus obtained at a scan rate of 10 mV s$^{-1}$. The capacitance increases for *ca.* 20% compared to the initial value after 2000 cycles (Fig. 8C), suggesting the excellent electrochemical stability of the hybrid carbon electrode.

### 7.3 Fuel cells

Unlike batteries or supercapacitors, which store energy chemically in the electrochemical cells, the fuel cell generates electricity *via* reactions between a fuel (anode) and an oxidant (cathode), which are continuously supplied from external
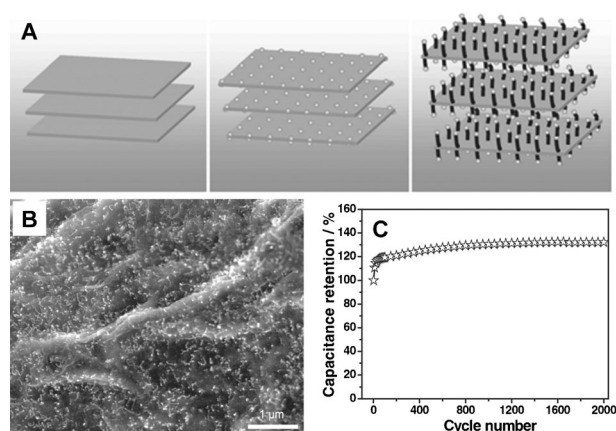


**Fig. 8** (A) Schematic illustration of the formation of hybrid materials with CNTs grown in between graphene nanosheets, showing stacked layers of GO (left), catalyst particles adhered onto layer surface after deposition (middle), and CNTs in between graphene layers after growth (right). (B) SEM image of the CGS sheet. (C) Variations of specific capacitance *versus* the cycle number measured at a scan rate of 200 mV s$^{-1}$ in 6 M KOH within the potential range from $-0.2$ to 0.45 V (*versus* saturated calomel electrode (SCE)). Reproduced with permission from ref. 53. Copyright 2010, John Wiley & Sons, Inc.

sources. There are several different combinations of the fuel and oxidant, with typical examples including the hydrogen/oxygen cell and the methanol/oxygen cell. Pt-based catalysts are the most popular materials used for low-temperature fuel cells, *e.g.* the oxidation of hydrogen, methanol, or reformate.[249] Since Pt is very expensive, Pt loading must be minimized, but the fuel cell performance cannot be compromised. Therefore, carbon-based catalyst supports, such as carbon black, CNTs and graphene, are used to provide good dispersity and thus large effective surface area of the supported catalyst particles. Graphene–Pt composites have been attempted in the fuel cells, such as the methanol oxidation cells[60–62,250–252] and the oxygen reduction cells.[63,253,254]

Enhanced electrocatalytic activity in methanol oxidation has been obtained in graphene-supported Pt catalysts as compared to the commercial carbon black (Vulcan XC-72) supported Pt NPs.[60,61] The superior performance arises from the large specific surface area of graphene and its high conductivity for electron and ion transport. Graphene has also shown advantages compared to the CNT-based catalyst support. First, the 2D configuration of graphene sheets with both sides exposed to the solution, leading to larger active surface area compared to the 1D tube structures. Second, due to the large curvature of the CNT walls, the deposited Pt particles are sometimes aggregated, and not as uniformly distributed as on graphene-based supports.[250] Moreover, it is demonstrated that the chemically converted graphene, or rGO, displays better tolerance towards CO poisoning during the methanol oxidation compared to CNTs, because the residual oxygenated functional groups of rGO can react and remove the carbonaceous species.[250] In a recent report, Yoo *et al.* found that graphene nanosheets (GNS) are able to assist the formation of Pt clusters with a size of $\sim 0.5$ nm,[251] and because these clusters are well distributed on the GNS surface, their aggregation into larger Pt particles is avoided.

In addition, based on a theoretical study, surface defects and voids on the graphene surface can enhance the interaction between the graphene and anchored Pt or Au clusters.[255] Consequently, these sub-nanometre Pt clusters can remain stable on GNS even after the heat treatment at 400 °C in an Ar/H$_2$ environment. The resulting Pt–GNS hybrid catalyst shows unusually high activity for methanol oxidation, e.g. the Pt–GNS exhibits a current density of 0.12 mA cm$^{-2}$ at 0.6 V (versus reference hydrogen electrode), about 3 times higher than that obtained with the Pt–carbon black catalyst.

Nitrogen-doped graphene sheets, with better conductivity compared to un-doped ones,[256] have also been used as catalyst supports in fuel cells.[62,63] The N-doped rGO can be prepared by nitrogen plasma treatment of rGO,[63] or thermal reduction of GO in the presence of ammonia (NH$_3$),[62] which gives rise to nitrogen species on the carbon basal plane, such as amino, pyridine and graphitic type groups. The presence of the nitrogen species results in a good coverage and dispersion of the in situ synthesized Pt NPs compared to the un-doped rGO surface. This advantage along with the N-doping induced increase of the electronic conductivity[256] has led to much enhanced electrocatalytic activities of N-rGO–Pt catalysts.[62,63] For example, in a methanol fuel cell, the N-doped rGO–Pt catalyst exhibited an oxidation current of 135 mA mg$^{-1}$, which is 2 times higher than that of the rGO–Pt catalyst.[62]

## 7.4 Photovoltaic devices

A photovoltaic device converts the solar energy into electricity. Besides the widely commercialized Si based solar cells, cheap and efficient alternatives, such as the polymer based solar cells, dye (or quantum dots, QD) sensitized solar cells, have also been intensively investigated. The following context will discuss the incorporation of graphene into these devices.

### 7.4.1 Silicon based solar cells.
In order to partially replace silicon, thus reducing cost in solar cell devices, carbon based materials have been attempted in the p-type amorphous carbon/n-type silicon (p-AC/n-Si) heterojunctions,[257] and CNT/Si heterojunctions.[258] However, amorphous carbon usually encounters difficulties in tuning its electronic properties, while the CNT-based thin film suffers from bundling and thus reduces the film connectivity and conductivity. In contrast, graphene-based films can be prepared with controlled thickness, good surface continuity, and tunable properties via doping, covalent or non-covalent functionalizations. CVD-grown graphene sheets with sizes of tens to hundreds micrometres have been deposited on n-Si with 100% coverage to make the Schottky junction solar cell,[64] which shows an efficiency (PCE, η) of up to ~1.5% with a fill factor of ~56% (FF, actual obtainable maximum power vs. the theoretical power). In addition to its low cost, the graphene film serves as a semitransparent electrode and an antireflection coating for the graphene/n-Si solar cells, and helps to generate a built-in voltage of 0.55–0.57 V for the effective electron-hole separation.[64,259] Although the obtained efficiency is still lower than that of pure Si-based solar cells, it is suggested that the efficiency can be increased in future by improving the conductivity and transparency of the graphene film.[64] Additionally, the tunable work function of the graphene layer

affords the additional advantage to the graphene/silicon solar cells, since a desirable work function allows for the efficient carrier injection at the interface. One way to adjust the work function of the graphene film is through controlling the layer number of the graphene sheets via the LbL deposition,[260] which has shown a sequential increase in work function with increasing layer numbers. Another effective way to control the work function is via chemical doping, e.g. Au-doping through the electrochemical deposition.[261] The resulting Au-doped graphene films exhibit a change in work function of up to ~0.5 eV (i.e. from −4.66 eV to −3.96 eV), which leads to more than 40 times increase in PCE as compared to the un-doped graphene films.

### 7.4.2 Polymer based solar cells.
In polymer-based heterojunction solar cells, graphene-based materials have been composited and incorporated to function as the electrodes,[19,33,217,262–264] electron transporters/acceptors,[225,265–267] and hole transporters.[218]

*a. Transparent electrodes.* Graphene thin films with easy accessibility, good flexibility and transparency have shown promises to replace indium tin oxide (ITO) as the transparent electrode for solar cells and other electronic devices. In a typical fabrication process, GO solutions are spin-coated on quartz substrate and reduced chemically followed by high temperature annealing. Additional layers in the device configuration are deposited on top of the rGO film in sequence to give the organic (e.g. quartz/rGO/P3HT/PCBM/PEDOT:PSS/LiF/Al)[217] or organic/inorganic hybrid (e.g. quartz/rGO/ZnO/P3HT/PEDOT:PSS/Au)[19] photovoltaic devices (Fig. 9A). High temperature annealing not only improves the conductivity of the rGO film,[217,264] but also increases the work function of rGO, resulting in a better match between the Fermi-level of the rGO layer and the conduction band of the adjacent
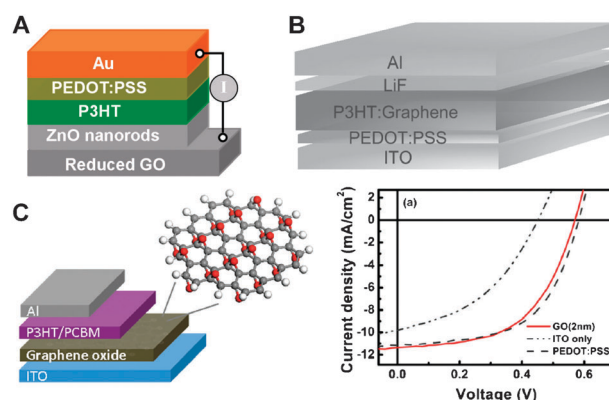


**Fig. 9** (A) Schematic illustration of the rGO thin film used as the transparent electrode in a ZnO/P3HT hybrid solar cell. Reproduced with permission from ref. 19. Copyright 2010, John Wiley & Sons, Inc. (B) Schematic illustration of the P3HT/graphene hybrid film used as the electron transport/acceptor layer in a polymer solar cell. Reproduced with permission from ref. 267. Copyright 2009, John Wiley & Sons, Inc. (C) Left: schematic illustration of GO used as the hole transport layer in a polymer solar cell. Right: Current–voltage characteristics of photovoltaic devices with no hole transport layer (curve labeled as ITO), with a 30 nm PEDOT:PSS layer, and a 2 nm thick GO film. Reproduced with permission from ref. 218. Copyright 2010, American Chemical Society.

semiconducting layer for efficient charge injection.[19] Besides the work function, another key concern for the rGO electrode is the transmittance. It is found that there exists a critical value for the transmittance of the rGO electrode (e.g. 65% in a device with a configuration of rGO/PEDOT:PSS/P3HT:PCBM/TiO$_2$/Al),[33] above which the performance of the device mainly depends on the charge transport efficiency through the rGO electrodes, and below which the performance is dominated by the light transmission efficiency. In addition to rGO films, CVD-grown graphene films with better electrical conductivity have also been used as the transparent electrode. The performance of the CVD-grown graphene anode can be improved by modulating its work function through chemical means such as ozone treatment or non-covalent functionalization.[262] In the former approach, although ozone treatment can generate the OH and C=O groups on the graphene surface, thus improving the open circuit voltage ($V_{oc}$) and PCE, the electronic conductivity is compromised due to the disrupted sp$^2$ network, which results in the decreased FF. In contrast, the non-covalent functionalization not only retains the good conductivity of CVD-grown graphene, but also increases the $V_{oc}$ and FF. For example, the functionalization of CVD-grown graphene with pyrene buanoic acid succidymidyl ester (PBASE) can adjust the work function of the graphene film from −4.2 to −4.7 eV, resulting in the increased $V_{oc}$, FF, and PCE with values of 0.55 V, 51.3%, and 1.71%, respectively (with a device configuration of glass/PBASE-graphene/PEDOT:PSS/P3HT:PCBM/LiF/Al).[262] Moreover, graphene films can be deposited/transferred onto flexible substrates, which presents as another advantage compared to the conventional ITO electrode.[33,263] For example, the organic solar cell with graphene film deposited on polyethylene terephthalate (PET) as the electrode can be operated under bending condition with a bending angle of up to 138°, whereas the ITO-based solar cell, with a comparable value of PCE, shows cracks under bending of only 60°.[263]

*b. Electron transport/acceptors.* One of the most important components in a polymer-based photovoltaic cell is the electron donor/acceptor layer (or the heterojunction), which contains a conjugated polymer (e.g. poly(3-hexylthiophene, P3HT) to generate electron–hole pairs upon photon absorption, and an acceptor with a relatively high electron affinity to dissociate the electron–hole pairs into separate charges. Fullerene and its derivatives (e.g. phenyl-C61-butyric acid, PCBM) are among the mostly employed acceptor materials due to their high electron affinity and charge mobility. The combination of P3HT and PCBM have been studied intensively in various configurations and the cell efficiencies of up to ~6% have been achieved.[265] However, the electron transport in the heterojunction is hindered due to problems associated with the phase separation process used to make the polymeric heterojunction, such as the isolated domains and structural traps. These problems have limited the obtained maximum efficiency in the polymer-based solar cells.[266] Graphene-based materials are anticipated to be used for the effective electron–hole separation and charge transport when blended with conjugated polymers, owing to its large surface area for donor/acceptor interfaces and continuous pathway for the

electron transfer.[225,267–269] For example, P3HT can be covalently functionalized on GO, and then mixed with C$_{60}$ to form the donor/acceptor heterojunction. The resulting GO-P3HT/C$_{60}$ based solar cell outperforms the P3HT/C$_{60}$ based cell with two times increase in PCE.[225] Alternatively, C$_{60}$-grafted graphene can be mixed with P3HT and applied as the acceptor layer.[269] Also, the isocyanate-modified GO sheets have been directly mixed with P3HT and function as the electron acceptor (Fig. 9B). In this work, the thermal annealing has played an important role in tuning the work function of the functionalized rGO for efficient charge carrier injection. When annealed at 160 °C for 20 min, the resulting P3HT/isocyanate-rGO based solar cell shows a maximum PCE of ~ 1.1%.

*c. Hole transport layers.* Direct connection of the electron donor/acceptor layer between the cathode and anode will result in the fast recombination of charge carriers and current leakage. Therefore, a hole transport layer is usually incorporated in between the anode and the electron donor/acceptor layer, such as the commonly used poly(3,4-ethylene-dioxythiophene) : poly(styrenesulfonate) (PEDOT:PSS). GO film has been shown as a simple and effective alternative to PEDOT:PSS in polymer-based solar cells.[218] In the configuration of glass/PBASE-ITO/GO/P3HT:PCBM/Al, the GO film with a band gap of ~3.6 eV is able to hinder the electron transport from the PCBM LUMO to the ITO anode, while bridging the holes to the anode. GO thin film with a thickness of ~2 nm has shown the best performance, since thicker films lead to larger resistance and reduced transmittance. The best PCE value obtained with the 2 nm GO film is ~3.5%, which is comparable to ~3.6% obtained in the PEDOT:PSS based solar cells (Fig. 9C).

**7.4.3 Dye sensitized solar cells (DSSCs).** Dye sensitized solar cells (DSSCs), in contrast to the solid state solar cells, usually consist of a layer of semiconducting materials deposited on the anode, e.g. TiO$_2$, covered with photo-sensitive dyes, and connected to a platinum cathode *via* an electrolyte. Upon light irradiation, the dye molecules are excited to inject electrons into the conduction band of the semiconductor layer. In DSSCs, it is important to increase the loading of dye molecules, enlarge the interface area of dye/electrolyte, and improve the conductivity of electrons at the semiconductor layer to compete with charge recombination. Therefore, besides being used as the transparent electrode in DSSCs,[270,271] the graphene derivatives have also been composited with TiO$_2$ nanostructures to enhance the above-mentioned factors. One of the benefits of rGO incorporation is that the work function of rGO (about −4.4 eV) is between the conduction band of TiO$_2$ and the work function of ITO, which allows for the fast collection of electrons at the anode to suppress charge recombination.[160] Importantly, on the basis of a theoretical study,[272] valence electrons might be directly excited under the visible light irradiation from graphene into the TiO$_2$ conduction band at the graphene/TiO$_2$ interface, giving rise to separated electron–hole pairs. In addition, the conductive percolation threshold of the rGO/TiO$_2$ layer is only at ~1 vol% of the rGO loading.[161] However, increasing

the rGO content compromises the transmittance of the composite film, hence an optimal value is to be determined to maximize the device efficiency.[156,161] Besides the enhanced conductivity, the large surface area of rGO improves the loading and dispersion of the dye molecules. It is reported that dye molecules, *e.g.* porphyrin, can directly bind to rGO surfaces, and upon photo-irradiation undergo energy and electron transfer to generate the photo-current.[273] Moreover, the rGO/TiO$_2$ composite forms a porous network, resulting in enhancement of light scattering at the photoanode.[161] Consequently, by using rGO/TiO$_2$ as the photoanode, a PCE of about 4–7% is obtained, which is at least 39% higher as compared to the commercial P25 TiO$_2$.[156,161]

**7.4.4 Quantum dots-based solar cells.** In addition to the silicon solar cells, polymer based solar cells and DSSCs, graphene has also been hybridized with quantum dots (QDs) to make photovoltaic devices. A novel layered graphene/CdS QD structure on ITO has been developed *via* electrophoretic and chemical bath deposition (Fig. 10A).[180] When the device contains eight repeating graphene/CdS QD bilayers, a surprisingly high PCE value of 16% is achieved (Fig. 10B), which outperforms all other carbon/QD based photovoltaic devices with the reported PCE value of ∼5%. The layered structure is believed to be critical in achieving the fast electron transfer from the QDs to the graphene acceptor and suppressing charge recombination. For comparison, a layered SWCNT/CdS-QD hybrid device was constructed in the same way, which shows a PCE of ∼9% (Fig. 10B). The reason why the graphene based device shows better performance compared to the one based on SWCNTs is because the graphene provides a better template for loading QDs, and the work function of graphene (∼ −4.2 eV) compared to that of SWCNTs (∼ −4.8 eV) energetically favors the direct electron transfer to the ITO electrode (with a work function of ∼ −4.8 eV).

### 7.5 Photocatalysis

In a photocatalysis reaction, the light induced electron–hole pairs formed on the catalyst surfaces (*e.g.* TiO$_2$), instead of being collected by an electrode, are directly scavenged by chemical reactions. Graphene/TiO$_2$ composites have shown an enhanced catalytic efficiency compared to TiO$_2$ alone in reactions such as water-splitting,[274] degradation of methylene

blue (MB),[67–69] and decomposition of 2,4-dichlorophenoxy-acetic acid (2,4-D).[275] These enhanced performances are attributed to the large surface area of graphene derivatives for loading of catalysts, and the excellent conductivity for electron capture and transport. However, compared to CNT-based composites, graphene-based composites in photo-catalysis have not shown the evident advantages, except for the low cost.[113] This is in contrast to the case of photovoltaic applications mentioned above. One of the possible reasons is that in photovoltaic devices, the composite films are connected to an external circuit for the electron transport and collection. The reliable process for making continuously graphene-based thin films, compared to CNT-based films, affords the continuous electron pathway and fast electron collection at the electrode.[64,180] However, in photocatalysis, the electron transfer to external circuit is not required.

### 7.6 Raman enhancement

Resonant Raman scattering (RRS) and surface enhanced Raman scattering (SERS) are important techniques to characterize material structures based on the Raman spectroscopy. The RRS requires the excitation wavelength in resonance with the electronic transition of the molecule, while the SERS mainly relies on the rough surface or nanoparticle films of noble metals such as Au and Ag. Recently, graphene-enhanced Raman scattering has attracted much research interest.[70–72] It is found that the enhancement of the absorbed molecules on graphene mainly comes from the fluorescent quenching effect due to the resonance energy transfer, which considerably reduces the background noise.[70] Meanwhile, the charge transfer between the molecules and graphene results in a chemical enhancement (or the chemical mechanism, CM).[71] This chemical enhancement, rather than the electromagnetic mechanism (EM), is confirmed by a systematic study of graphene-enhanced scattering of surface absorbed proto-porphyrin IX (PPP). This work shows that the first layer of PPP on graphene contributes to most of the enhancement, and the enhancement increases when the functional group of PPP becomes closer to the graphene surface.[72] However, the CM-based enhancement is orders weaker compared to the EM-based one. As a result, the combination of fluorescence quenching of graphene and the EM enhancement from noble metals is expected to lead to even superior enhancement of Raman signals. This concept has been demonstrated in Raman substrates made from graphene/Au NPs[144,145,276,277] and graphene/Au film,[278] where the composite substrates have shown better Raman enhancement compared to the graphene film (GO or rGO) or NPs alone. In the case of graphene/NP based Raman substrates, the particle loading, or the density of NPs on graphene-based templates, is important for the enhancement of signals. Two ways have been demonstrated to increase the particle loading. One is to use GO sheets with abundant functional groups as the nucleation sites for the *in situ* synthesis of NPs. The other is to use the microwave-synthesized 3D graphitic petal arrays with large specific surface area as the template for synthesis of NPs (Fig. 11).[276]

Moreover, it has been demonstrated that the Raman signals of graphene or functionalized graphene (GO or rGO) can be
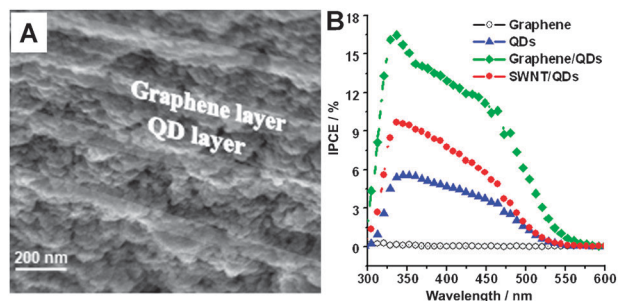


**Fig. 10** (A) Cross-sectional SEM image of a layered graphene/QDs sample. (B) Dependence of the incident photon conversion efficiency (IPCE, external quantum yield) on the incident wavelength of different photoelectrodes. Reproduced with permission from ref. 180. Copyright 2010, John Wiley & Sons, Inc.
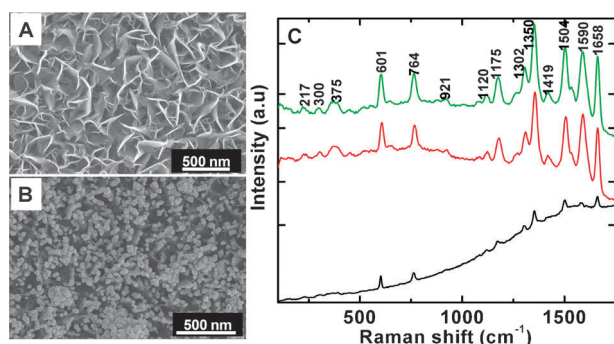
**Fig. 11** SEM images of (A) graphitic petals and (B) Au NP-decorated petals. (C) Raman spectra of $10^{-5}$ (black curve), $10^{-6}$ (red curve) and $10^{-7}$ M (green curve) R6G on Au-decorated graphitic petals. Reproduced with permission from ref. 276. Copyright 2010, American Institute of Physics.

greatly enhanced by the anchored metal nanostructures.[142,185,279] For example, *in situ* synthesized Ag NPs can enhance the Raman signals of the D and G bands of GO with one order of enhancement (up to 16 folds).[279] Similarly, snowflake-shaped Au structures deposited on rGO have shown the Raman enhancement of rGO;[142] and Au nanorod can give rise to enhanced Raman signals of rGO by 34 folds at the rod tip.[185]

## 8. Conclusions and outlook

The collection of many useful properties of graphene and its derivatives, along with the low cost and availability for mass production, has made them promising building blocks in functional composites, incorporated with polymers, metals, metal oxides, organic crystals, and so on.

Various fabrication methods have been developed for preparation of graphene-based composites. Driven by the constant demand for optimization of composite properties, the particular efforts are directed towards the design and formation of specially constructed hybrid architectures rather than the random mixtures. Some examples are highlighted in this review, such as the graphene-encapsulated metal oxides for Li ion batteries, sandwiched graphene/CNT structures for supercapacitors, and layered graphene/quantum dots for solar cells. More versatile fabrication/synthesis strategies are expected to be developed in future for the continuous advancement of functional composites.

To date, graphene-based fillers have brought about enhanced electrical, thermal and mechanical properties to graphene–polymer composites, which outperform many types of traditional filler materials. These advantages of graphene-based fillers arise from their large surface area for effective electrical/heat conduction and load transfer, and the 2D functionable surfaces for the strong filler/matrix interaction.

Other types of graphene-based composites, involving conductive polymers, transition metal oxides, and noble metals, are attractive candidates in the electrochemical energy conversion and storage based applications, such as the Li ion batteries, supercapacitors and fuel cells, with recent achievement in enhanced performances and anticipated commercialization in the near future.

Another promising area for graphene-based composites lies in various strategies for harvesting of solar energy, like organic–inorganic hybrid solar cells and photocatalysis. Flexible and transparent electrodes based on graphene thin films have been used to grow semiconductor nanostructures, which are directly incorporated in photovoltaic devices, in order to place the conventional but expensive ITO electrodes to realize high efficiency for photo-conversion at relatively low cost. In other investigations, graphene-based composite films have also functioned as the electron transport/acceptor layer, hole transport layer and so on. Despite the huge efforts, the significant breakthrough in harvesting solar energy has not been achieved in laboratory trials and remains the key challenge for future exploitation.

## References

1 K. S. Novoselov, A. K. Geim, S. V. Morozov, D. Jiang, Y. Zhang, S. V. Dubonos, I. V. Grigorieva and A. A. Firsov, *Science*, 2004, **306**, 666–669.
2 M. D. Stoller, S. Park, Y. Zhu, J. An and R. S. Ruoff, *Nano Lett.*, 2008, **8**, 3498–3502.
3 R. R. Nair, P. Blake, A. N. Grigorenko, K. S. Novoselov, T. J. Booth, T. Stauber, N. M. R. Peres and A. K. Geim, *Science*, 2008, **320**, 1308–1308.
4 C. Lee, X. D. Wei, J. W. Kysar and J. Hone, *Science*, 2008, **321**, 385–388.
5 A. A. Balandin, S. Ghosh, W. Bao, I. Calizo, D. Teweldebrhan, F. Miao and C. N. Lau, *Nano Lett.*, 2008, **8**, 902–907.
6 K. S. Kim, Y. Zhao, H. Jang, S. Y. Lee, J. M. Kim, K. S. Kim, J.-H. Ahn, P. Kim, J.-Y. Choi and B. H. Hong, *Nature*, 2009, **457**, 706–710.
7 X. S. Li, W. W. Cai, J. H. An, S. Kim, J. Nah, D. X. Yang, R. Piner, A. Velamakanni, I. Jung, E. Tutuc, S. K. Banerjee, L. Colombo and R. S. Ruoff, *Science*, 2009, **324**, 1312–1314.
8 P. W. Sutter, J. I. Flege and E. A. Sutter, *Nat. Mater.*, 2008, **7**, 406–411.
9 N. Xiao, X. Dong, L. Song, D. Liu, Y. Tay, S. Wu, L.-J. Li, Y. Zhao, T. Yu, H. Zhang, W. Huang, H. H. Hng, P. M. Ajayan and Q. Yan, *ACS Nano*, 2011, **5**, 2749–2755.
10 D. Li, M. B. Muller, S. Gilje, R. B. Kaner and G. G. Wallace, *Nat. Nanotechnol.*, 2008, **3**, 101–105.
11 Y. Hernandez, V. Nicolosi, M. Lotya, F. M. Blighe, Z. Y. Sun, S. De, I. T. McGovern, B. Holland, M. Byrne, Y. K. Gun'ko, J. J. Boland, P. Niraj, G. Duesberg, S. Krishnamurthy, R. Goodhue, J. Hutchison, V. Scardaci, A. C. Ferrari and J. N. Coleman, *Nat. Nanotechnol.*, 2008, **3**, 563–568.
12 C. Vallés, C. Drummond, H. Saadaoui, C. A. Furtado, M. He, O. Roubeau, L. Ortolani, M. Monthioux and A. Pénicaud, *J. Am. Chem. Soc.*, 2008, **130**, 15802–15804.
13 M. Lotya, Y. Hernandez, P. J. King, R. J. Smith, V. Nicolosi, L. S. Karlsson, F. M. Blighe, S. De, Z. Wang, I. T. McGovern, G. S. Duesberg and J. N. Coleman, *J. Am. Chem. Soc.*, 2009, **131**, 3611–3620.
14 X. Qi, K.-Y. Pu, H. Li, X. Zhou, S. Wu, Q.-L. Fan, B. Liu, F. Boey, W. Huang and H. Zhang, *Angew. Chem., Int. Ed.*, 2010, **49**, 9426–9429.
15 Q. He, H. G. Sudibya, Z. Yin, S. Wu, H. Li, F. Boey, W. Huang, P. Chen and H. Zhang, *ACS Nano*, 2010, **4**, 3201–3208.

16  B. Li, X. Cao, H. G. Ong, J. W. Cheah, X. Zhou, Z. Yin, H. Li, J. Wang, F. Boey, W. Huang and H. Zhang, *Adv. Mater.*, 2010, **22**, 3058–3061.

17  X. Qi, K. Y. Pu, X. Zhou, H. Li, B. Liu, F. Boey, W. Huang and H. Zhang, *Small*, 2010, **6**, 663–669.

18  S. Wu, Z. Yin, Q. He, X. Huang, X. Zhou and H. Zhang, *J. Phys. Chem. C*, 2010, **114**, 11816–11821.

19  Z. Yin, S. Wu, X. Zhou, X. Huang, Q. Zhang, F. Boey and H. Zhang, *Small*, 2010, **6**, 307–312.

20  X. Zhou, X. Huang, X. Qi, S. Wu, C. Xue, F. Y. C. Boey, Q. Yan, P. Chen and H. Zhang, *J. Phys. Chem. C*, 2009, **113**, 10842–10846.

21  X. Zhou, Y. Wei, Q. He, F. Boey, Q. Zhang and H. Zhang, *Chem. Commun.*, 2010, **46**, 6974–6976.

22  J. Liu, Z. Yin, X. Cao, F. Zhao, A. Lin, L. Xie, Q. Fan, F. Boey, H. Zhang and W. Huang, *ACS Nano*, 2010, **4**, 3987–3992.

23  W. S. Hummers and R. E. Offeman, *J. Am. Chem. Soc.*, 1958, **80**, 1339–1339.

24  G. Lu, X. Zhou, H. Li, Z. Yin, B. Li, L. Huang, F. Boey and H. Zhang, *Langmuir*, 2010, **26**, 6164–6166.

25  B. Li, G. Lu, X. Zhou, X. Cao, F. Boey and H. Zhang, *Langmuir*, 2009, **25**, 10455–10458.

26  X. Cao, Q. He, W. H. Shi, B. Li, Z. Y. Zeng, Y. Shi, Q. Yan and H. Zhang, *Small*, 2011, **9**, 1199–1202.

27  X. Huang, Z. Y. Yin, S. X. Wu, X. Y. Qi, Q. Y. He, Q. C. Zhang, Q. Y. Yan, F. Boey and H. Zhang, *Small*, 2011, **7**, 1876–1902.

28  H. Li, J. Zhang, X. Zhou, G. Lu, Z. Yin, G. Li, T. Wu, F. Boey, S. S. Venkatraman and H. Zhang, *Langmuir*, 2009, **26**, 5603–5609.

29  X. Zhou, G. Lu, X. Qi, S. Wu, H. Li, F. Boey and H. Zhang, *J. Phys. Chem. C*, 2009, **113**, 19119–19122.

30  Z. Wang, J. Zhang, P. Chen, X. Zhou, Y. Yang, S. Wu, L. Niu, Y. Han, L. H. Wang, P. Chen, F. Boey, Q. C. Zhang, B. Liedberg and H. Zhang, *Biosens. Bioelectron.*, 2011, **26**, 3881–3886.

31  D. Li, M. B. Muller, S. Gilje, R. B. Kaner and G. G. Wallace, *Nat. Nanotechnol.*, 2008, **3**, 101–105.

32  I. K. Moon, J. Lee, R. S. Ruoff and H. Lee, *Nat. Commun.*, 2010, **1**, 73.

33  Z. Yin, S. Y. Sun, T. Salim, S. Wu, X. Huang, Q. He, Y. M. Lam and H. Zhang, *ACS Nano*, 2010, **4**, 5263–5268.

34  H. G. Sudibya, Q. He, H. Zhang and P. Chen, *ACS Nano*, 2011, **5**, 1990–1994.

35  R. Muszynski, B. Seger and P. V. Kamat, *J. Phys. Chem. C*, 2008, **112**, 5263–5266.

36  W. Shi, J. Zhu, D. H. Sim, Y. Y. Tay, Z. Y. Lu, X. J. Zhang, H. Zhang, H. H. Hng and Q. Yan, *J. Mater. Chem.*, 2011, **21**, 3422–3427.

37  J. Zhu, T. Zhu, X. Zhou, Y. Zhang, X. W. Lou, X. Chen, H. Chen, H. Zhang, H. H. Hng, J. Ma and Q. Yan, *Nanoscale*, 2011, **3**, 1084–1089.

38  X. Huang, S. Li, Y. Huang, S. Wu, X. Zhou, S. Li, C. L. Gan, F. Boey, C. A. Mirkin and H. Zhang, *Nat. Commun.*, 2011, **2**, 292.

39  S. Wang, B. M. Goh, K. K. Manga, Q. Bao, P. Yang and K. P. Loh, *ACS Nano*, 2010, **4**, 6180–6186.

40  T. H. Han, W. J. Lee, D. H. Lee, J. E. Kim, E. Y. Choi and S. O. Kim, *Adv. Mater.*, 2010, **22**, 2060–2064.

41  H. F. Yang, Q. X. Zhang, C. S. Shan, F. H. Li, D. X. Han and L. Niu, *Langmuir*, 2010, **26**, 6708–6712.

42  T. Ramanathan, A. A. Abdala, S. Stankovich, D. A. Dikin, M. Herrera-Alonso, R. D. Piner, D. H. Adamson, H. C. Schniepp, X. Chen, R. S. Ruoff, S. T. Nguyen, I. A. Aksay, R. K. Prud'homme and L. C. Brinson, *Nat. Nanotechnol.*, 2008, **3**, 327–331.

43  M. Jahan, Q. Bao, J.-X. Yang and K. P. Loh, *J. Am. Chem. Soc.*, 2010, **132**, 14487–14495.

44  C. Petit and T. J. Bandosz, *Adv. Funct. Mater.*, 2010, **20**, 111–118.

45  C. Petit, J. Burress and T. J. Bandosz, *Carbon*, 2011, **49**, 563–572.

46  C. H. Lu, H. H. Yang, C. L. Zhu, X. Chen and G. N. Chen, *Angew. Chem., Int. Ed.*, 2009, **121**, 4879–4881.

47  H. Chang, L. Tang, Y. Wang, J. Jiang and J. Li, *Anal. Chem.*, 2010, **82**, 2341–2346.

48  Y. Wang, Z. Li, D. Hu, C.-T. Lin, J. Li and Y. Lin, *J. Am. Chem. Soc.*, 2010, **132**, 9274–9276.

49  X. Dong, B. Li, A. Wei, X. Cao, M. B. Chan-Park, H. Zhang, L.-J. Li, W. Huang and P. Chen, *Carbon*, 2011, **49**, 2944–2949.

50  V. C. Tung, L.-M. Chen, M. J. Allen, J. K. Wassei, K. Nelson, R. B. Kaner and Y. Yang, *Nano Lett.*, 2009, **9**, 1949–1955.

51  E. Yoo, J. Kim, E. Hosono, H.-s. Zhou, T. Kudo and I. Honma, *Nano Lett.*, 2008, **8**, 2277–2282.

52  D. Yu and L. Dai, *J. Phys. Chem. Lett.*, 2009, **1**, 467–470.

53  Z. Fan, J. Yan, L. Zhi, Q. Zhang, T. Wei, J. Feng, M. Zhang, W. Qian and F. Wei, *Adv. Mater.*, 2010, **22**, 3723–3728.

54  Z.-S. Wu, W. Ren, L. Wen, L. Gao, J. Zhao, Z. Chen, G. Zhou, F. Li and H.-M. Cheng, *ACS Nano*, 2010, **4**, 3187–3194.

55  S. Yang, X. Feng, S. Ivanovici and K. Müllen, *Angew. Chem., Int. Ed.*, 2010, **49**, 8408–8411.

56  H. Wang, L.-F. Cui, Y. Yang, H. Sanchez Casalongue, J. T. Robinson, Y. Liang, Y. Cui and H. Dai, *J. Am. Chem. Soc.*, 2010, **132**, 13978–13980.

57  Y. Zhang, H. Li, L. Pan, T. Lu and Z. Sun, *J. Electroanal. Chem.*, 2009, **634**, 68–71.

58  F. Li, J. Song, H. Yang, S. Gan, Q. Zhang, D. Han, A. Ivaska and L. Niu, *Nanotechnology*, 2009, **20**, 455602.

59  F. Kim, J. Luo, R. Cruz-Silva, L. J. Cote, K. Sohn and J. Huang, *Adv. Funct. Mater.*, 2010, **20**, 2867–2873.

60  Y. Li, L. Tang and J. Li, *Electrochem. Commun.*, 2009, **11**, 846–849.

61  L. Dong, R. R. S. Gari, Z. Li, M. M. Craig and S. Hou, *Carbon*, 2010, **48**, 781–787.

62  L.-S. Zhang, X.-Q. Liang, W.-G. Song and Z.-Y. Wu, *Phys. Chem. Chem. Phys.*, 2010, **12**, 12055–12059.

63  R. I. Jafri, N. Rajalakshmi and S. Ramaprabhu, *J. Mater. Chem.*, 2010, **20**, 7114–7117.

64  X. Li, H. Zhu, K. Wang, A. Cao, J. Wei, C. Li, Y. Jia, Z. Li, X. Li and D. Wu, *Adv. Mater.*, 2010, **22**, 2743–2748.

65  J. Song, Z. Yin, Z. Yang, P. Amaladass, S. Wu, J. Ye, Y. Zhao, W. Deng, H. Zhang and X. Liu, *Chem. Eur. J.*, 2011, DOI: 10.1002/chem.201101263.

66  H. Liu, S. Ryu, Z. Chen, M. L. Steigerwald, C. Nuckolls and L. E. Brus, *J. Am. Chem. Soc.*, 2009, **131**, 17099–17101.

67  J. Liu, H. Bai, Y. Wang, Z. Liu, X. Zhang and D. D. Sun, *Adv. Funct. Mater.*, 2010, **20**, 4175–4181.

68  J. Du, X. Lai, N. Yang, J. Zhai, D. Kisailus, F. Su, D. Wang and L. Jiang, *ACS Nano*, 2010, **5**, 590–596.

69  H. Zhang, X. J. Lv, Y. M. Li, Y. Wang and J. H. Li, *ACS Nano*, 2010, **4**, 380–386.

70  L. Xie, L. Ling, Y. Fang, J. Zhang and Z. Liu, *J. Am. Chem. Soc.*, 2009, **131**, 9890–9891.

71  X. Ling, L. Xie, Y. Fang, H. Xu, H. Zhang, J. Kong, M. S. Dresselhaus, J. Zhang and Z. Liu, *Nano Lett.*, 2009, **10**, 553–561.

72  X. Ling and J. Zhang, *Small*, 2010, **6**, 2020–2025.

73  X. Du, I. Skachko, A. Barker and E. Y. Andrei, *Nat. Nanotechnol.*, 2008, **3**, 491–495.

74  K. S. Novoselov, A. K. Geim, S. V. Morozov, D. Jiang, M. I. Katsnelson, I. V. Grigorieva, S. V. Dubonos and A. A. Firsov, *Nature*, 2005, **438**, 197–200.

75  Y. B. Zhang, Y. W. Tan, H. L. Stormer and P. Kim, *Nature*, 2005, **438**, 201–204.

76  K. S. Novoselov, Z. Jiang, Y. Zhang, S. V. Morozov, H. L. Stormer, U. Zeitler, J. C. Maan, G. S. Boebinger, P. Kim and A. K. Geim, *Science*, 2007, **315**, 1379–1379.

77  X. Du, I. Skachko, F. Duerr, A. Luican and E. Y. Andrei, *Nature*, 2009, **462**, 192–195.

78  V. P. Gusynin, S. G. Sharapov and J. P. Carbotte, *Phys. Rev. Lett.*, 2006, **96**, 256802.

79  K. F. Mak, M. Y. Sfeir, Y. Wu, C. H. Lui, J. A. Misewich and T. F. Heinz, *Phys. Rev. Lett.*, 2008, **101**, 196405.

80  J. M. Dawlaty, S. Shivaraman, M. Chandrashekhar, F. Rana and M. G. Spencer, *Appl. Phys. Lett.*, 2008, **92**, 042116.

81  F. Wang, Y. Zhang, C. Tian, C. Girit, A. Zettl, M. Crommie and Y. R. Shen, *Science*, 2008, **320**, 206–209.

82  J. H. Seol, I. Jo, A. L. Moore, L. Lindsay, Z. H. Aitken, M. T. Pettes, X. Li, Z. Yao, R. Huang, D. Broido, N. Mingo, R. S. Ruoff and L. Shi, *Science*, 2010, **328**, 213–216.

83  Y. W. Gao and P. Hao, *Physica E*, 2009, **41**, 1561–1566.

84  O. Hod and G. E. Scuseria, *Nano Lett.*, 2009, **9**, 2619–2622.

85  O. Frank, G. Tsoukleri, J. Parthenios, K. Papagelis, I. Riaz, R. Jalil, K. S. Novoselov and C. Galiotis, *ACS Nano*, 2010, **4**, 3131–3138.

86 H. C. Schniepp, K. N. Kudin, J. L. Li, R. K. Prud'homme, R. Car, D. A. Saville and I. A. Aksay, *ACS Nano*, 2008, **2**, 2577–2584.

87 Y. Wang, X. Xu, J. Lu, M. Lin, Q. Bao, B. Özyilmaz and K. P. Loh, *ACS Nano*, 2010, **4**, 6146–6152.

88 C. Berger, Z. Song, T. Li, X. Li, A. Y. Ogbazghi, R. Feng, Z. Dai, A. N. Marchenkov, E. H. Conrad, P. N. First and W. A. de Heer, *J. Phys. Chem. B*, 2004, **108**, 19912–19916.

89 K. V. Emtsev, A. Bostwick, K. Horn, J. Jobst, G. L. Kellogg, L. Ley, J. L. McChesney, T. Ohta, S. A. Reshanov, J. Rohrl, E. Rotenberg, A. K. Schmid, D. Waldmann, H. B. Weber and T. Seyller, *Nat. Mater.*, 2009, **8**, 203–207.

90 M. Choucair, P. Thordarson and J. A. Stride, *Nat. Nanotechnol.*, 2009, **4**, 30–33.

91 X. Wang, L. Zhi, N. Tsao, Ž. Tomović, J. Li and K. Müllen, *Angew. Chem., Int. Ed.*, 2008, **47**, 2990–2992.

92 X. Yan, X. Cui and L.-s. Li, *J. Am. Chem. Soc.*, 2010, **132**, 5944–5945.

93 H.-P. Boehm and E. Stumpp, *Carbon*, 2007, **45**, 1381–1383.

94 S. Malik, A. Vijayaraghavan, R. Erni, K. Ariga, I. Khalakhan and J. P. Hill, *Nanoscale*, 2010, **2**, 2139–2143.

95 T. E. Weller, M. Ellerby, S. S. Saxena, R. P. Smith and N. T. Skipper, *Nat. Phys.*, 2005, **1**, 39–41.

96 N. Emery, C. Hérold, M. d'Astuto, V. Garcia, C. Bellin, J. F. Marêché, P. Lagrange and G. Loupias, *Phys. Rev. Lett.*, 2005, **95**, 087003.

97 M. S. Dresselhaus and G. Dresselhaus, *Adv. Phys.*, 2002, **51**, 1–186.

98 X. L. Li, G. Y. Zhang, X. D. Bai, X. M. Sun, X. R. Wang, E. Wang and H. J. Dai, *Nat. Nanotechnol.*, 2008, **3**, 538–542.

99 N. Liu, F. Luo, H. Wu, Y. Liu, C. Zhang and J. Chen, *Adv. Funct. Mater.*, 2008, **18**, 1518–1525.

100 A. Lerf, H. He, M. Forster and J. Klinowski, *J. Phys. Chem. B*, 1998, **102**, 4477–4482.

101 W. Gao, L. B. Alemany, L. Ci and P. M. Ajayan, *Nat. Chem.*, 2009, **1**, 403–408.

102 S. Wu, Z. Yin, Q. He, G. Lu, X. Zhou and H. Zhang, *J. Mater. Chem.*, 2010, **21**, 3467–3470.

103 S. Agarwal, X. Zhou, F. Ye, Q. He, G. C. K. Chen, J. Soo, F. Boey, H. Zhang and P. Chen, *Langmuir*, 2010, **26**, 2244–2247.

104 J. Liu, Z. Lin, T. Liu, Z. Yin, X. Zhou, S. Chen, L. Xie, F. Boey, H. Zhang and W. Huang, *Small*, 2010, **6**, 1536–1542.

105 W. Hu, C. Peng, W. Luo, M. Lv, X. Li, D. Li, Q. Huang and C. Fan, *ACS Nano*, 2010, **4**, 4317–4323.

106 L. Zhang, X. Li, Y. Huang, Y. Ma, X. Wan and Y. Chen, *Carbon*, 2010, **48**, 2367–2371.

107 Y. Wang, Z. Shi, Y. Huang, Y. Ma, C. Wang, M. Chen and Y. Chen, *J. Phys. Chem. C*, 2009, **113**, 13103–13107.

108 X. Lv, Y. Huang, Z. Liu, J. Tian, Y. Wang, Y. Ma, J. Liang, S. Fu, X. Wan and Y. Chen, *Small*, 2009, **5**, 1682–1687.

109 X. Fan, W. Peng, Y. Li, X. Li, S. Wang, G. Zhang and F. Zhang, *Adv. Mater.*, 2008, **20**, 4490–4493.

110 V. Dua, S. Surwade, S. Ammu, S. Agnihotra, S. Jain, K. Roberts, S. Park, R. Ruoff and S. Manohar, *Angew. Chem., Int. Ed.*, 2010, **49**, 2154–2157.

111 J. B. Liu, S. H. Fu, B. Yuan, Y. L. Li and Z. X. Deng, *J. Am. Chem. Soc.*, 2010, **132**, 7279–7281.

112 Q. He, S. Wu, S. Gao, X. Cao, Z. Yin, H. Li, P. Chen and H. Zhang, *ACS Nano*, 2011, **5**, 5038–5044.

113 G. Williams, B. Seger and P. V. Kamat, *ACS Nano*, 2008, **2**, 1487–1491.

114 X. Huang, X. Z. Zhou, S. X. Wu, Y. Y. Wei, X. Y. Qi, J. Zhang, F. Boey and H. Zhang, *Small*, 2010, **6**, 513–516.

115 Y. Matsumoto, M. Koinuma, S. Y. Kim, Y. Watanabe, T. Taniguchi, K. Hatakeyama, H. Tateishi and S. Ida, *ACS Appl. Mater. Interfaces*, 2010, **2**, 3461–3466.

116 Y. H. Ng, A. Iwase, A. Kudo and R. Amal, *J. Phys. Chem. Lett.*, 2010, **1**, 2607–2612.

117 M. J. McAllister, J. L. Li, D. H. Adamson, H. C. Schniepp, A. A. Abdala, J. Liu, M. Herrera-Alonso, D. L. Milius, R. Car, R. K. Prud'homme and I. A. Aksay, *Chem. Mater.*, 2007, **19**, 4396–4404.

118 C. Mattevi, G. Eda, S. Agnoli, S. Miller, K. A. Mkhoyan, O. Celik, D. Mastrogiovanni, G. Granozzi, E. Garfunkel and M. Chhowalla, *Adv. Funct. Mater.*, 2009, **19**, 2577–2583.

119 Z. Lin, Y. Yao, Z. Li, Y. Liu, Z. Li and C.-P. Wong, *J. Phys. Chem. C*, 2010, **114**, 14819–14825.

120 S. Mao, G. Lu, K. Yu, Z. Bo and J. Chen, *Adv. Mater.*, 2010, **22**, 3521–3526.

121 Y. W. Zhu, M. D. Stoller, W. W. Cai, A. Velamakanni, R. D. Piner, D. Chen and R. S. Ruoff, *ACS Nano*, 2010, **4**, 1227–1233.

122 J. Wu, M. Agrawal, H. c. A. Becerril, Z. Bao, Z. Liu, Y. Chen and P. Peumans, *ACS Nano*, 2009, **4**, 43–48.

123 H. A. Becerril, J. Mao, Z. Liu, R. M. Stoltenberg, Z. Bao and Y. Chen, *ACS Nano*, 2008, **2**, 463–470.

124 C. D. Zangmeister, *Chem. Mater.*, 2010, **22**, 5625–5629.

125 V. Abdelsayed, S. Moussa, H. M. Hassan, H. S. Aluri, M. M. Collinson and M. S. El-Shall, *J. Phys. Chem. Lett.*, 2010, **1**, 2804–2809.

126 L. J. Cote, R. Cruz-Silva and J. X. Huang, *J. Am. Chem. Soc.*, 2009, **131**, 11027–11032.

127 K. Vinodgopal, B. Neppolian, I. V. Lightcap, F. Grieser, M. Ashokkumar and P. V. Kamat, *J. Phys. Chem. Lett.*, 2010, **1**, 1987–1993.

128 H. M. A. Hassan, V. Abdelsayed, A. Khder, K. M. AbouZeid, J. Terner, M. S. El-Shall, S. I. Al-Resayes and A. A. El-Azhary, *J. Mater. Chem.*, 2009, **19**, 3832–3837.

129 Z. Wang, X. Zhou, J. Zhang, F. Boey and H. Zhang, *J. Phys. Chem. C*, 2009, **113**, 14071–14075.

130 M. Zhou, Y. Wang, Y. Zhai, J. Zhai, W. Ren, F. Wang and S. Dong, *Chem.–Eur. J.*, 2009, **15**, 6116–6120.

131 H.-L. Guo, X.-F. Wang, Q.-Y. Qian, F.-B. Wang and X.-H. Xia, *ACS Nano*, 2009, **3**, 2653–2659.

132 G. K. Ramesha and S. Sampath, *J. Phys. Chem. C*, 2009, **113**, 7985–7989.

133 M. J. Fernández-Merino, L. Guardia, J. I. Paredes, S. Villar-Rodil, P. Solís-Fernández, A. Martínez-Alonso and J. M. D. Tascón, *J. Phys. Chem. C*, 2010, **114**, 6426–6432.

134 E. C. Salas, Z. Sun, A. Lüttge and J. M. Tour, *ACS Nano*, 2010, **4**, 4852–4856.

135 S. Pei, J. Zhao, J. Du, W. Ren and H.-M. Cheng, *Carbon*, 2010, **48**, 4466–4474.

136 G. Eda, Y. Y. Lin, C. Mattevi, H. Yamaguchi, H. A. Chen, I. S. Chen, C. W. Chen and M. Chhowalla, *Adv. Mater.*, 2010, **22**, 505–509.

137 X. Yan, B. Li, X. Cui, Q. Wei, K. Tajima and L.-S. Li, *J. Phys. Chem. Lett.*, 2011, **2**, 1119–1124.

138 S. Stankovich, D. A. Dikin, G. H. B. Dommett, K. M. Kohlhaas, E. J. Zimney, E. A. Stach, R. D. Piner, S. T. Nguyen and R. S. Ruoff, *Nature*, 2006, **442**, 282–286.

139 F. H. Li, H. F. Yang, C. S. Shan, Q. X. Zhang, D. X. Han, A. Ivaska and L. Niu, *J. Mater. Chem.*, 2009, **19**, 4022–4025.

140 H. M. A. Hassan, V. Abdelsayed, A. Khder, K. M. AbouZeid, J. Terner, M. S. El-Shall, S. I. Al-Resayes and A. A. El-Azhary, *J. Mater. Chem.*, 2009, **19**, 3832–3837.

141 C. Xu, X. Wang and J. W. Zhu, *J. Phys. Chem. C*, 2008, **112**, 19841–19845.

142 K. Jasuja and V. Berry, *ACS Nano*, 2009, **3**, 2358–2366.

143 Y.-K. Kim, H.-K. Na and D.-H. Min, *Langmuir*, 2010, **26**, 13065–13070.

144 G. Goncalves, P. Marques, C. M. Granadeiro, H. I. S. Nogueira, M. K. Singh and J. Gracio, *Chem. Mater.*, 2009, **21**, 4796–4802.

145 J. Huang, L. Zhang, B. Chen, N. Ji, F. Chen, Y. Zhang and Z. Zhang, *Nanoscale*, 2010, **2**, 2733–2738.

146 J. Liu, S. Fu, B. Yuan, Y. Li and Z. Deng, *J. Am. Chem. Soc.*, 2010, **132**, 7279–7281.

147 G. H. Lu, S. Mao, S. Park, R. S. Ruoff and J. H. Chen, *Nano Res.*, 2009, **2**, 192–200.

148 J. F. Shen, M. Shi, N. Li, B. Yan, H. W. Ma, Y. Z. Hu and M. X. Ye, *Nano Res.*, 2010, **3**, 339–349.

149 P. V. Kamat, *J. Phys. Chem. Lett.*, 2010, **1**, 520–527.

150 T. Cassagneau and J. H. Fendler, *J. Phys. Chem. B*, 1999, **103**, 1789–1793.

151 G. M. Scheuermann, L. Rumi, P. Steurer, W. Bannwarth and R. Mulhaupt, *J. Am. Chem. Soc.*, 2009, **131**, 8262–8270.

152 J. L. Johnson, A. Behnam, S. J. Pearton and A. Ural, *Adv. Mater.*, 2010, **22**, 4877–4880.

153 Y. C. Si and E. T. Samulski, *Chem. Mater.*, 2008, **20**, 6792–6797.

154 H. Wang, J. T. Robinson, G. Diankov and H. Dai, *J. Am. Chem. Soc.*, 2010, **132**, 3270–3271.

155 D. Marquardt, C. Vollmer, R. Thomann, P. Steurer, R. Mülhaupt, E. Redel and C. Janiak, *Carbon*, 2011, **49**, 1326–1332.

156 N. L. Yang, J. Zhai, D. Wang, Y. S. Chen and L. Jiang, *ACS Nano*, 2010, **4**, 887–894.

157 D. Wang, D. Choi, J. Li, Z. Yang, Z. Nie, R. Kou, D. Hu, C. Wang, L. V. Saraf, J. Zhang, I. A. Aksay and J. Liu, *ACS Nano*, 2009, **3**, 907–914.

158 O. Akhavan, M. Abdolahad, A. Esfandiar and M. Mohatashamifar, *J. Phys. Chem. C*, 2010, **114**, 12955–12959.

159 B. Li, X. T. Zhang, X. H. Li, L. Wang, R. Y. Han, B. B. Liu, W. T. Zheng, X. L. Li and Y. C. Liu, *Chem. Commun.*, 2010, **46**, 3499–3501.

160 Y. B. Tang, C. S. Lee, J. Xu, Z. T. Liu, Z. H. Chen, Z. B. He, Y. L. Cao, G. D. Yuan, H. S. Song, L. M. Chen, L. B. Luo, H. M. Cheng, W. J. Zhang, I. Bello and S. T. Lee, *ACS Nano*, 2010, **4**, 3482–3488.

161 S. R. Sun, L. Gao and Y. Q. Liu, *Appl. Phys. Lett.*, 2010, **96**, 083113.

162 Y. Zhang, Z.-R. Tang, X. Fu and Y.-J. Xu, *ACS Nano*, 2010, **4**, 7303–7314.

163 J. O. Hwang, D. H. Lee, J. Y. Kim, T. H. Han, B. H. Kim, M. Park, K. No and S. O. Kim, *J. Mater. Chem.*, 2010, **21**, 3432–3437.

164 J. M. Lee, Y. B. Pyun, J. Yi, J. W. Choung and W. I. Park, *J. Phys. Chem. C*, 2009, **113**, 19134–19138.

165 G. Williams and P. V. Kamat, *Langmuir*, 2009, **25**, 13869–13873.

166 D. Wang, R. Kou, D. Choi, Z. Yang, Z. Nie, J. Li, L. V. Saraf, D. Hu, J. Zhang, G. L. Graff, J. Liu, M. A. Pope and I. A. Aksay, *ACS Nano*, 2010, **4**, 1587–1595.

167 L. S. Zhang, L. Y. Jiang, H. J. Yan, W. D. Wang, W. Wang, W. G. Song, Y. G. Guo and L. J. Wan, *J. Mater. Chem.*, 2010, **20**, 5462–5467.

168 S. Chen, J. Zhu, X. Wu, Q. Han and X. Wang, *ACS Nano*, 2010, **4**, 2822–2830.

169 J. Yan, Z. Fan, T. Wei, W. Qian, M. Zhang and F. Wei, *Carbon*, 2010, **48**, 3825–3833.

170 J. Yan, T. Wei, W. Qiao, B. Shao, Q. Zhao, L. Zhang and Z. Fan, *Electrochim. Acta*, 2010, **55**, 6973–6978.

171 J. Zhu, Y. K. Sharma, Z. Zeng, X. Zhang, M. Srinivasan, S. Mhaisalkar, H. Zhang, H. H. Hng and Q. Yan, *J. Phys. Chem. C*, 2011, **115**, 8400–8406.

172 J. F. Shen, Y. Z. Hu, M. Shi, N. Li, H. W. Ma and M. X. Ye, *J. Phys. Chem. C*, 2010, **114**, 1498–1503.

173 G. Zhou, D.-W. Wang, F. Li, L. Zhang, N. Li, Z.-S. Wu, L. Wen, G. Q. Lu and H.-M. Cheng, *Chem. Mater.*, 2010, **22**, 5306–5313.

174 J. Liang, Y. Xu, D. Sui, L. Zhang, Y. Huang, Y. Ma, F. Li and Y. Chen, *J. Phys. Chem. C*, 2010, **114**, 17465–17471.

175 X. Yang, X. Zhang, Y. Ma, Y. Huang, Y. Wang and Y. Chen, *J. Mater. Chem.*, 2009, **19**, 2710–2714.

176 J. Y. Son, Y.-H. Shin, H. Kim and H. M. Jang, *ACS Nano*, 2010, **4**, 2655–2658.

177 C. Xu, X. Wang, L. C. Yang and Y. P. Wu, *J. Solid State Chem.*, 2009, **182**, 2486–2490.

178 S. Watcharotone, D. A. Dikin, S. Stankovich, R. Piner, I. Jung, G. H. B. Dommett, G. Evmenenko, S. E. Wu, S. F. Chen, C. P. Liu, S. T. Nguyen and R. S. Ruoff, *Nano Lett.*, 2007, **7**, 1888–1892.

179 M. Feng, R. Q. Sun, H. B. Zhan and Y. Chen, *Nanotechnology*, 2010, **21**, 075601.

180 C. X. Guo, H. B. Yang, Z. M. Sheng, Z. S. Lu, Q. L. Song and C. M. Li, *Angew. Chem., Int. Ed.*, 2010, **49**, 3014–3017.

181 A. Cao, Z. Liu, S. Chu, M. Wu, Z. Ye, Z. Cai, Y. Chang, S. Wang, Q. Gong and Y. Liu, *Adv. Mater.*, 2010, **22**, 103–106.

182 C. Nethravathi, T. Nisha, N. Ravishankar, C. Shivakumara and M. Rajamathi, *Carbon*, 2009, **47**, 2054–2059.

183 Y. T. Kim, J. H. Han, B. H. Hong and Y. U. Kwon, *Adv. Mater.*, 2010, **22**, 515–518.

184 Y. Lin, K. Zhang, W. Chen, Y. Liu, Z. Geng, J. Zeng, N. Pan, L. Yan, X. Wang and J. G. Hou, *ACS Nano*, 2010, **4**, 3033–3038.

185 Y.-K. Kim, H.-K. Na, Y. W. Lee, H. Jang, S. W. Han and D.-H. Min, *Chem. Commun.*, 2010, **46**, 3185–3187.

186 S. Guo, S. Dong and E. Wang, *ACS Nano*, 2009, **4**, 547–555.

187 I. V. Lightcap, T. H. Kosel and P. V. Kamat, *Nano Lett.*, 2010, **10**, 577–583.

188 H. C. Choi, M. Shim, S. Bangsaruntip and H. Dai, *J. Am. Chem. Soc.*, 2002, **124**, 9058–9059.

189 H. Q. Zhou, C. Y. Qiu, Z. Liu, H. C. Yang, L. J. Hu, J. Liu, H. F. Yang, C. Z. Gu and L. F. Sun, *J. Am. Chem. Soc.*, 2010, **132**, 944–946.

190 K. Jasuja, J. Linn, S. Melton and V. Berry, *J. Phys. Chem. Lett.*, 2010, **1**, 1853–1860.

191 Y. X. Xu, W. J. Hong, H. Bai, C. Li and G. Q. Shi, *Carbon*, 2009, **47**, 3538–3543.

192 T. Ramanathan, S. Stankovich, D. A. Dikin, H. Liu, H. Shen, S. T. Nguyen and L. C. Brinson, *J. Polym. Sci., Part B: Polym. Phys.*, 2007, **45**, 2097–2112.

193 D. Y. Cai and M. Song, *Nanotechnology*, 2009, **20**, 315708.

194 D. Y. Cai, K. Yusoh and M. Song, *Nanotechnology*, 2009, **20**, 085712.

195 Q. Wu, Y. X. Xu, Z. Y. Yao, A. R. Liu and G. Q. Shi, *ACS Nano*, 2010, **4**, 1963–1970.

196 I. H. Kim and Y. G. Jeong, *J. Polym. Sci., Part B: Polym. Phys.*, 2010, **48**, 850–858.

197 H. B. Zhang, W. G. Zheng, Q. Yan, Y. Yang, J. W. Wang, Z. H. Lu, G. Y. Ji and Z. Z. Yu, *Polymer*, 2010, **51**, 1191–1196.

198 A. Dasari, Z.-Z. Yu and Y.-W. Mai, *Polymer*, 2009, **50**, 4112–4121.

199 A. P. Yu, P. Ramesh, M. E. Itkis, E. Bekyarova and R. C. Haddon, *J. Phys. Chem. C*, 2007, **111**, 7565–7569.

200 X. C. Xiao, T. Xie and Y. T. Cheng, *J. Mater. Chem.*, 2010, **20**, 3508–3514.

201 M. A. Rafiee, J. Rafiee, I. Srivastava, Z. Wang, H. H. Song, Z. Z. Yu and N. Koratkar, *Small*, 2010, **6**, 179–183.

202 X. S. Zhou, T. B. Wu, B. J. Hu, G. Y. Yang and B. X. Han, *Chem. Commun.*, 2010, **46**, 3663–3665.

203 K. Zhang, L. L. Zhang, X. S. Zhao and J. S. Wu, *Chem. Mater.*, 2010, **22**, 1392–1401.

204 J. Yan, T. Wei, B. Shao, Z. J. Fan, W. Z. Qian, M. L. Zhang and F. Wei, *Carbon*, 2010, **48**, 487–493.

205 H. L. Wang, Q. L. Hao, X. J. Yang, L. D. Lu and X. Wang, *ACS Appl. Mater. Interfaces*, 2010, **2**, 821–828.

206 H. L. Wang, Q. L. Hao, X. J. Yang, L. D. Lu and X. Wang, *Electrochem. Commun.*, 2009, **11**, 1158–1161.

207 D. W. Wang, F. Li, J. P. Zhao, W. C. Ren, Z. G. Chen, J. Tan, Z. S. Wu, I. Gentle, G. Q. Lu and H. M. Cheng, *ACS Nano*, 2009, **3**, 1745–1752.

208 R. Verdejo, F. Barroso-Bujans, M. A. Rodriguez-Perez, J. A. de Saja and M. A. Lopez-Manchado, *J. Mater. Chem.*, 2008, **18**, 2221–2226.

209 H. Hu, X. Wang, J. Wang, L. Wan, F. Liu, H. Zheng, R. Chen and C. Xu, *Chem. Phys. Lett.*, 2010, **484**, 247–253.

210 T. Wei, G. L. Luo, Z. J. Fan, C. Zheng, J. Yan, C. Z. Yao, W. F. Li and C. Zhang, *Carbon*, 2009, **47**, 2296–2299.

211 J. Liang, Y. Huang, L. Zhang, Y. Wang, Y. Ma, T. Guo and Y. Chen, *Adv. Funct. Mater.*, 2009, **19**, 2297–2302.

212 J. Liang, Y. Xu, Y. Huang, L. Zhang, Y. Wang, Y. Ma, F. Li, T. Guo and Y. Chen, *J. Phys. Chem. C*, 2009, **113**, 9921–9927.

213 J. Liang, Y. Wang, Y. Huang, Y. Ma, Z. Liu, J. Cai, C. Zhang, H. Gao and Y. Chen, *Carbon*, 2009, **47**, 922–925.

214 A. A. Balandin, S. Ghosh, W. Bao, I. Calizo, D. Teweldebrhan, F. Miao and C. N. Lau, *Nano Lett.*, 2008, **8**, 902–907.

215 D. D. Kulkarni, I. Choi, S. S. Singamaneni and V. V. Tsukruk, *ACS Nano*, 2010, **4**, 4667–4676.

216 X. Zhao, Q. Zhang, Y. Hao, Y. Li, Y. Fang and D. Chen, *Macromolecules*, 2010, **43**, 9411–9416.

217 Y. Xu, G. Long, L. Huang, Y. Huang, X. Wan, Y. Ma and Y. Chen, *Carbon*, 2010, **48**, 3308–3311.

218 S. S. Li, K. H. Tu, C. C. Lin, C. W. Chen and M. Chhowalla, *ACS Nano*, 2010, **4**, 3169–3174.

219 L. Valentini, M. Cardinali, S. B. Bon, D. Bagnis, R. Verdejo, M. A. Lopez-Manchado and J. M. Kenny, *J. Mater. Chem.*, 2010, **20**, 995–1000.

220 H. J. Salavagione, M. n. A. Gómez and G. Martínez, *Macromolecules*, 2009, **42**, 6331–6334.

221 Z. Liu, J. T. Robinson, X. Sun and H. Dai, *J. Am. Chem. Soc.*, 2008, **130**, 10876–10877.

222 A. Midya, V. Mamidala, J. X. Yang, P. K. L. Ang, Z. K. Chen, W. Ji and K. P. Loh, *Small*, 2010, **6**, 2292–2300.

223 M. Fang, K. G. Wang, H. B. Lu, Y. L. Yang and S. Nutt, *J. Mater. Chem.*, 2010, **20**, 1982–1992.

224 X. D. Zhuang, Y. Chen, G. Liu, P. P. Li, C. X. Zhu, E. T. Kang, K. G. Noeh, B. Zhang, J. H. Zhu and Y. X. Li, *Adv. Mater.*, 2010, **22**, 1731–1735.

225 D. Yu, Y. Yang, M. Durstock, J.-B. Baek and L. Dai, *ACS Nano*, 2010, **4**, 5633–5640.

226 Y. Lin, J. Jin and M. Song, *J. Mater. Chem.*, 2011, **21**, 3455–3461.

227 J. Björk, F. Hanke, C.-A. Palma, P. Samori, M. Cecchini and M. Persson, *J. Phys. Chem. Lett.*, 2010, **1**, 3407–3412.

228 S. Stankovich, R. D. Piner, X. Chen, N. Wu, S. T. Nguyen and R. S. Ruoff, *J. Mater. Chem.*, 2006, **16**, 155–158.

229 M. R. Palacin, *Chem. Soc. Rev.*, 2009, **38**, 2565–2575.

230 J. M. Tarascon and M. Armand, *Nature*, 2001, **414**, 359–367.

231 M. S. Whittingham, *Science*, 1976, **192**, 1126–1127.

232 J. N. Reimers and J. R. Dahn, *J. Electrochem. Soc.*, 1992, **139**, 2091–2097.

233 M. M. Thackeray, J. T. Vaughey, C. S. Johnson, A. J. Kropf, R. Benedek, L. M. L. Fransson and K. Edstrom, *J. Power Sources*, 2003, **113**, 124–130.

234 Y.-G. Guo, J.-S. Hu and L.-J. Wan, *Adv. Mater.*, 2008, **20**, 2878–2887.

235 A. S. Arico, P. Bruce, B. Scrosati, J.-M. Tarascon and W. van Schalkwijk, *Nat. Mater.*, 2005, **4**, 366–377.

236 N. A. Kaskhedikar and J. Maier, *Adv. Mater.*, 2009, **21**, 2664–2680.

237 H. Kim, S.-W. Kim, Y.-U. Park, H. Gwon, D.-H. Seo, Y. Kim and K. Kang, *Nano Res.*, 2010, **3**, 813–821.

238 Y. Qiu, K. Yan, S. Yang, L. Jin, H. Deng and W. Li, *ACS Nano*, 2010, **4**, 6515–6526.

239 I. A. Courtney and J. R. Dahn, *J. Electrochem. Soc.*, 1997, **144**, 2045–2052.

240 C. o. S. P. E. Systems and N. R. C. (U.S.), Meeting the Energy Needs of Future Warriors, National Academies Press, 2004.

241 B. E. Conway, *Electrochemical Supercapacitors: Scientific Fundamentals and Technological Applications*, Kulwer Academic/Plenum Press, New York, 1999.

242 C. Liu, F. Li, L.-P. Ma and H.-M. Cheng, *Adv. Mater.*, 2010, **22**, E28–E62.

243 Z.-S. Wu, W. Ren, D.-W. Wang, F. Li, B. Liu and H.-M. Cheng, *ACS Nano*, 2010, **4**, 5835–5842.

244 G. A. Snook, P. Kao and A. S. Best, *J. Power Sources*, 2011, **196**, 1–12.

245 K. S. Ryu, Y.-G. Lee, Y.-S. Hong, Y. J. Park, X. Wu, K. M. Kim, M. G. Kang, N.-G. Park and S. H. Chang, *Electrochim. Acta*, 2004, **50**, 843–847.

246 M. Mastragostino, C. Arbizzani and F. Soavi, *J. Power Sources*, 2001, **97–98**, 812–815.

247 J. Yan, T. Wei, Z. J. Fan, W. Z. Qian, M. L. Zhang, X. D. Shen and F. Wei, *J. Power Sources*, 2010, **195**, 3041–3045.

248 J. Xu, K. Wang, S.-Z. Zu, B.-H. Han and Z. Wei, *ACS Nano*, 2010, **4**, 5019–5026.

249 S. Srinivasan, R. Mosdale, P. Stevens and C. Yang, *Annu. Rev. Energy Environ.*, 1999, **24**, 281–328.

250 Y. Li, W. Gao, L. Ci, C. Wang and P. M. Ajayan, *Carbon*, 2010, **48**, 1124–1130.

251 E. Yoo, T. Okata, T. Akita, M. Kohyama, J. Nakamura and I. Honma, *Nano Lett.*, 2009, **9**, 2255–2259.

252 S. Liu, J. Wang, J. Zeng, J. Ou, Z. Li, X. Liu and S. Yang, *J. Power Sources*, 2010, **195**, 4628–4633.

253 Y. Y. Shao, S. Zhang, C. M. Wang, Z. M. Nie, J. Liu, Y. Wang and Y. H. Lin, *J. Power Sources*, 2010, **195**, 4600–4605.

254 B. Seger and P. V. Kamat, *J. Phys. Chem. C*, 2009, **113**, 7990–7995.

255 Y. Okamoto, *Chem. Phys. Lett.*, 2006, **420**, 382–386.

256 L. S. Panchakarla, K. S. Subrahmanyam, S. K. Saha, A. Govindaraj, H. R. Krishnamurthy, U. V. Waghmare and C. N. R. Rao, *Adv. Mater.*, 2009, **21**, 4726–4730.

257 Z. Q. Ma and B. X. Liu, *Sol. Energy Mater. Sol. Cells*, 2001, **69**, 339–344.

258 Y. Jia, J. Wei, K. Wang, A. Cao, Q. Shu, X. Gui, Y. Zhu, D. Zhuang, G. Zhang, B. Ma, L. Wang, W. Liu, Z. Wang, J. Luo and D. Wu, *Adv. Mater.*, 2008, **20**, 4594–4598.

259 R. Won, *Nat. Photonics*, 2010, **4**, 411.

260 K. Ihm, J. T. Lim, K. J. Lee, J. W. Kwon, T. H. Kang, S. Chung, S. Bae, J. H. Kim, B. H. Hong and G. Y. Yeom, *Appl. Phys. Lett.*, 2010, **97**, 032113.

261 Y. M. Shi, K. K. Kim, A. Reina, M. Hofmann, L. J. Li and J. Kong, *ACS Nano*, 2010, **4**, 2689–2694.

262 Y. Wang, X. Chen, Y. Zhong, F. Zhu and K. P. Loh, *Appl. Phys. Lett.*, 2009, **95**, 063302.

263 L. Gomez De Arco, Y. Zhang, C. W. Schlenker, K. Ryu, M. E. Thompson and C. Zhou, *ACS Nano*, 2010, **4**, 2865–2873.

264 Q. Su, S. Pang, V. Alijani, C. Li, X. Feng and K. Müllen, *Adv. Mater.*, 2009, **21**, 3191–3195.

265 J. Peet, J. Y. Kim, N. E. Coates, W. L. Ma, D. Moses, A. J. Heeger and G. C. Bazan, *Nat. Mater.*, 2007, **6**, 497–500.

266 J. J. Dittmer, E. A. Marseglia and R. H. Friend, *Adv. Mater.*, 2000, **12**, 1270–1274.

267 Q. Liu, Z. Liu, X. Zhang, L. Yang, N. Zhang, G. Pan, S. Yin, Y. Chen and J. Wei, *Adv. Funct. Mater.*, 2009, **19**, 894–904.

268 Z. Liu, Q. Liu, Y. Huang, Y. Ma, S. Yin, X. Zhang, W. Sun and Y. Chen, *Adv. Mater.*, 2008, **20**, 3924–3930.

269 D. Yu, K. Park, M. Durstock and L. Dai, *J. Phys. Chem. Lett.*, 2011, **2**, 1113–1118.

270 L. Kavan, J. H. Yum and M. Grätzel, *ACS Nano*, 2010, **5**, 165–172.

271 J. D. Roy-Mayhew, D. J. Bozym, C. Punckt and I. A. Aksay, *ACS Nano*, 2010, **4**, 6203–6211.

272 A. Du, Y. H. Ng, N. J. Bell, Z. Zhu, R. Amal and S. C. Smith, *J. Phys. Chem. Lett.*, 2011, **2**, 894–899.

273 A. Wojcik and P. V. Kamat, *ACS Nano*, 2010, **4**, 6697–6706.

274 X. Y. Zhang, H. P. Li, X. L. Cui and Y. H. Lin, *J. Mater. Chem.*, 2010, **20**, 2801–2806.

275 Y. H. Ng, I. V. Lightcap, K. Goodwin, M. Matsumura and P. V. Kamat, *J. Phys. Chem. Lett.*, 2010, **1**, 2222–2227.

276 C. S. Rout, A. Kumar, G. Xiong, J. Irudayaraj and T. S. Fisher, *Appl. Phys. Lett.*, 2010, **97**, 133108.

277 G. Lu, H. Li, C. Liusman, Z. Yin, S. Wu and H. Zhang, *Chem. Sci.*, 2011, DOI: 10.1039/C1SC00254F.

278 Y. Wang, Z. Ni, H. Hu, Y. Hao, C. P. Wong, T. Yu, J. T. L. Thong and Z. X. Shen, *Appl. Phys. Lett.*, 2010, **97**, 163111.

279 C. Xu and X. Wang, *Small*, 2009, **5**, 2212–2217.